

**Basal Conditions of Petermann Glacier and Jakobshavn Isbrae derived from
Airborne Ice Penetrating Radar Measurements**

by

Manjish Adhikari

Submitted to the graduate degree program in Electrical Engineering and the Graduate Faculty of
the University of Kansas in partial fulfillment of the requirements for the degree of Master of
Science.

Chairperson Dr. Carl Leuschen

Co - Chairperson Dr. Jilu Li

Dr. Christopher Allen

Dr. John Paden

Date of Defense: 30 August 2018

The Thesis Committee for Manjish Adhikari
certifies that this is the approved version of the following thesis:

**Basal Conditions of Petermann Glacier and Jakobshavn Isbrae
derived from Airborne Ice Penetrating Radar Measurements**

Chairperson Dr. Carl Leuschen

Co - Chairperson Dr. Jilu Li

Date Approved: 30 August 2018

Abstract

Understanding ice dynamics and ice basal conditions is important because of their impacts on sea level rise. Radio echo sounding has been extensively used for characterizing the ice sheets. The radar reflectivity of the ice bed is of special importance because it can discriminate frozen and thawed ice beds. The knowledge of the spatial distribution of basal water is crucial in explaining the flow velocity and stability of glaciers and ice sheets. Basal echo reflectivity used to identify the areas of basal melting can be calculated by compensating ice bed power for geometric losses, rough interface losses, system losses and englacial attenuation.

Two important outlet glaciers of Greenland, Petermann glacier and Jakobshavn isbrae have been losing a lot of ice mass in recent years, and are therefore studied to derive its basal conditions from airborne radar surveys in this thesis.

The ice surface and bed roughness of these glaciers are estimated using Radar Statistical Reconnaissance (RSR) method and validated using roughness derived from NASA's Airborne Topographic Mapper (ATM) and Ku band altimeter. Englacial attenuation is modeled using Schroeder's variable attenuation method. After compensating for these losses, the basal reflectivity for the two glaciers is estimated and validated using cross over analysis, geophysics, hydraulic potential, abruptive index and coherence index.

The areas of basal melting i.e. areas with higher reflectivity are identified. Petermann glacier is found to have alternate frozen and thawed regions explaining the process of ice movement by friction and freezing. Due to the lack of topographic pinning the glacier is subject to higher ice flow speed. Jakobshavn glacier has several areas of basal melting scattered in the catchment area with most concentration near the glacier front which is likely due to surface water

infiltration into ice beds via moulins and sinks. The ice bed channels and retrograde slope of this glacier are also important in routing subglacial water and ice mass. The basal conditions of these two glaciers presented in this study can help in modeling the behavior of these glaciers in the future.

Acknowledgements

First, I would like to thank my advisor Dr. Jilu Li, for introducing me to Radars and Ice sheet research. This work would not have been possible without his constant guidance. I am grateful to thank Dr. John Paden for helping me understand algorithms and radar signal processing. I would also like to thank Dr. Allen whose Radar classes helped me a lot and I still use it as a reference for most of the works. I am also grateful to Dr. Leuschen, Dr. Stiles, Dr. Blunt, Dr. Frost, and Dr. Prescott. I really enjoyed their classes and learned a lot of new and interesting things. I am grateful to my friends at KU who have always inspired me to continue in my research journey.

Finally, I would also like to thank all the staff, faculty and students at CReSIS for helping me through my Master's journey at KU.

Table of Contents

Chapter 1 Introduction.....	1
1.1 Background and Motivation	1
1.2 Thesis organization	4
Chapter 2 Theory and Methodology	5
2.1 Radar Equations	5
2.2 Roughness Estimation.....	8
2.2.1 Roughness Estimation from MCoRDS measurements using Radar Statistical Reconnaissance Method (RSR)	9
2.2.2 Roughness Estimation from ATM Measurements.....	13
2.2.3 Roughness Estimation from Ku band Altimeter Measurements.....	14
2.3 Englacial Attenuation Estimation	14
2.3.1 Layer Method.....	15
2.3.2 Constant Attenuation Model	16
2.3.3 Variable Attenuation Model	18
2.4 Ice bed Reflectivity and Basal Conditions.....	19
2.4.1 Interpretation of Basal Conditions	19
2.4.2 Abruptive Index	20
2.4.3 Coherence Index	20
Chapter 3 Study Areas and Data.....	22

3.1 Petermann glacier.....	22
3.2 Jakobshavn glacier	23
3.3 Radar Systems and Data	25
3.3.1 MCoRDS.....	25
3.3.2 Airborne Topographic Mapper (ATM).....	27
3.3.3 Ku Band Altimeter	28
Chapter 4 Results and Discussions.....	29
4.1 Application of RSR.....	29
4.2 Peterman Glacier Basal Conditions	31
4.2.1 Roughness Estimate of Peterman Glacier.....	31
4.2.2 Englacial Attenuation Estimation of Peterman Glacier	34
4.2.3 Ice Bed Reflectivity of Peterman Glacier	44
4.2.4 Discussion and validation of ice bed reflectivity result	45
4.3 Basal Conditions of Jakobshavn Glacier	53
4.3.1 Roughness Estimate for Jakobshavn Glacier.....	54
4.3.2 Ice Attenuation Estimation of Jakobshavn Glacier.....	56
4.3.3 Ice Bed Reflectivity of Jakobshavn Glacier.....	61
4.3.4 Discussion and validation of ice bed reflectivity result	63
Chapter 5 Summary and Conclusion.....	68
5.1 Summary	68

5.2 Conclusion and Future Works	69
References.....	84

List of Figures

Figure 2.1 Radar Echogram (left), A-scope with received signal power versus depth (right) (Allen, 2008)	6
Figure 2.2 Echogram with tracking of specular layers (Li, 2014)	15
Figure 2.3 Ice Attenuation Estimate using Layer Method (Li, 2014).....	16
Figure 3.1 Petermann glacier (Middleton, 2012).....	22
Figure 3.2 Petermann glacier ice tongue (Middleton, 2012)	23
Figure 3.3 Jakobshavn glacier (Middleton, 2012)	24
Figure 3.4 Airborne Topographic LIDAR (ATM) (NASA, 2009).....	27
Figure 4.1 Area used for Roughness Comparison and Verification	29
Figure 4.2 DMS pictures of areas with Smoother (a) and Rougher (b) Surfaces [29]. (c) and (d) Radar Echograms obtained from Ku-band altimeter showing corresponding smoother (a) and rougher areas (b)	30
Figure 4.3 Surface RMS heights obtained from MCoRDS (red), ATM (blue) and Ku-band altimeter (green).....	30
Figure 4.4 Radar Survey area of Petermann Glacier under Operation IceBridge (A), Bed Roughness calculated from MCoRDS (B), Surface Roughness calculated from MCoRDS (C), and Surface Roughness calculated from ATM (D).	32
Figure 4.5 . Surface RMS Height at Crevasse as seen from LANDSAT Imagery (Rough Location)	33
Figure 4.6 Ice Bed Power 2010 season (left) and 2011 season (right)	34
Figure 4.7 Histogram of Ice Bed Power for two seasons	35

Figure 4.8 Power Correction due to Surface Roughness (Left) and due to Bed Roughness (Right)	36
Figure 4.9 Geometrically corrected Relative Ice bed power for 2010 and 2011 season	36
Figure 4.10 Ice Bed Reflectivity using uniform attenuation rate (right), Total ice attenuation (left)	37
Figure 4.11 Range of Relative Reflectivity	37
Figure 4.12 Radar Line extending from ice interior to ice margin (a), Relative Ice Bed Power versus Depth profile (b), Apparent Attenuation (c), Ice Thickness (d), Modelled Attenuation (Red) and Apparent Attenuation (Blue) using variable attenuation method (e	39
Figure 4.13 Radar Survey Line (a), Ice Thickness Profile along the Survey Line (b), Relative Power along depth profile (c)	40
Figure 4.14 Attenuation Rate calculated from variable attenuation method	41
Figure 4.15 Attenuation Rates at Cross over Locations	42
Figure 4.16 Interpolation of Ice Attenuation rate from Crossover using different interpolation techniques	42
Figure 4.17 Attenuation Rate using interpolation method	43
Figure 4.18 Total Ice Attenuation (left), Depth (right)	43
Figure 4.19 Relative Ice Bed Reflectivity (left), Range of Relative Reflectivity Values (right)	44
Figure 4.20 Crossover Locations (left), Ice Bed Reflectivity Difference (Right)	45
Figure 4.21 Reflectivity difference at cross over locations	46
Figure 4.22 Echograms showing areas of basal melt	47
Figure 4.23 Ice Bed Reflectivity, Abruptive Index and Coherence Index for 20100324_01_03448	
Figure 4.24 Ice Bed Reflectivity from this study plotted over Ice Bed Elevation Map	49

Figure 4.25 Ice Bed Reflectivity from this study plotted over Ice Surface Speed Map (Joughin et al., 2010)	50
Figure 4.26 Abruptive Index Map (left) and Coherence Index Map(right) for Petermann Glacier	51
Figure 4.27 Areas of basal melting from this study (yellow) compared with previously identified areas of basal melting (red, Chu et al., 2016)	52
Figure 4.28 Survey Area with Radar Lines (top), Surface Roughness derived from MCoRDS (bottom).....	54
Figure 4.29 Surface Roughness overlaying Landsat Image at Jakobshavn	55
Figure 4.30 Ice Bed Roughness	56
Figure 4.31 Geometrically corrected ice bed power plotted with corresponding ice depth	57
Figure 4.32 Attenuation Rate at Jakobshavn using variable attenuation rate method	58
Figure 4.33 Attenuation Rate difference at crossover locations (left), Histogram of attenuation rate difference in dB/km at crossover locations (right)	59
Figure 4.34 Attenuation Rate (dB/km) across Jakobshavn Glacier applying linearly variable attenuation rate method.....	60
Figure 4.35 Total ice attenuation at Jakobshavn glacier.....	60
Figure 4.36 Ice Bed Reflectivity of Jakobshavn Glacier	61
Figure 4.37 Histogram showing range of relative ice bed reflectivity values	61
Figure 4.38 Areas of basal melt (red) in Jakobshavn Glacier, Purple dots show hydrological outlets (Lewis, 2009) and dotted lines show hydrological sub basin (Lewis, 2009).....	62
Figure 4.39 Relative Reflectivity Difference at crossovers (left), Relative Reflectivity Difference at crossovers (right).....	63

Figure 4.40 Echogram for 20080706_01_004	64
Figure 4.41 Ice Bed Reflectivity for 20080706_01_004	65
Figure 4.42 Abruptive Index for 20080706_01_004	65
Figure 4.43 Areas with basal melt (red) from this study on top of ice bed map (Bamber, 2013)	66

List of Tables

Table 1 MCoRDS System Parameters	26
Table 2 Ku band Altimeter Specifications.....	28
Table 3 Ice Bed Power Statistics	35

Chapter 1 Introduction

1.1 Background and Motivation

With the global climate change and temperature rise there is constant effect on the polar ice sheet thus making significant change in the rise of sea level. Greenland ice sheet mass loss has doubled in last two decades (Shephard et al., 2012) as a result of increased ice discharge into oceans and increased melting of ice sheets. This phenomenon contributes about 0.6mm per year global sea level rise (Shephard et al., 2012). Monitoring sea level change is important for different aspects as it threatens lives in coastal areas and islands.

Huge efforts have been made to study the ice sheet conditions especially the Antarctic and Greenland ice sheet which can bring about a significant change in the sea level rise. ICESat (Ice, Cloud, and land Elevation Satellite 2), is one of the NASA's missions for measuring ice sheet elevation and sea ice freeboard, in addition to land topography and vegetation characteristics (Schutz et al., 2005). Similarly, Operation IceBridge uses RADARs, LIDARS and other sensors to measure ice sheet conditions (Studinger et al., 2008). The large ice sheets of Greenland and Antarctica contain enough ice to contribute to a sea level rise of roughly 70 meters if all ice were to melt completely (Church et al., 2001).

Several models have been proposed to explain the ice sheet conditions and are constantly being used to explain the ice conditions such as SIMulation COde for POLythermal Ice Sheets (SICOPOLIS) (Greeve, 1997), Community Ice sheet model (Rutt et al., 2009), 3D full stokes Elmer model (Favier et al., 2011) and so on which are used to simulate the global climate model and the evolution of ice sheets. Ice sheet dynamics play important role in explaining the glaciers

and melting. Ice motion is affected by two main factors i.e. temperature and the conditions of the bases. A lot of ice breaks due to the melting of ice sheets both superficially as well as the basal melting. One of the necessary criteria for basal sliding is basal melt which is caused by different processes such as high pressure from thick ice sheet, geothermal flux (Dahl- Jensen et al., 2003), basal friction (van der Veen et al., 2013), surface water infiltration (Rennermalm et al., 2013), and so on. Ice sheet loss is then caused due to sliding of ice sheets into the oceans.

Ice core drilling (Dahl Jensen et al., 2003) and seismic analysis (Smith et al., 2009) have been used to understand the ice sheet conditions however it is not feasible to cover whole of the ice sheet and tend to require more time and effort in field. Airborne ice-sounding radar is more viable technique to effectively survey ice sheets, glaciers and their basal conditions at large scale.

Ice penetrating radars have been used to locate ice surface elevations and subglacial morphology (Rignot, 2013), ice beds (Bamber et al., 2013; Fretwell, 2013), internal layers (Kanagaratnam et al., 2004) and ultimately the thickness of ice sheet (Bamber, 2001). Apart from that many studies have also interpreted ice bed echoes to characterize the subglacial environments of ice sheets. Specifically, echo amplitude analyses have characterized the subglacial interface (Neal, 1979; Bentley et al., 1998), identified subglacial lakes (Oswald and Robin, 1973; Robin et al., 1977; Seroussi et al., 2013; Palmer et al., 2013; MacGregor et al., 2016) and also determined the ice sheet grounding lines (Uratsuka et al., 1996). Similarly, small scale roughness and slopes of the ice bed have been derived from ice bed echoes and received ice bed power. (Oswald, 1975; Neal, 1982).

A coherent radar system detects both the amplitude and phase of the radar signals and has a number of advantages over incoherent radar systems (Peters et al., 2005). The coherent

integration from a moving airborne platform forms a synthetic aperture radar (SAR) that improves along-track resolution, improves SNR and reduces along-track clutter (Peters et al., 2005). SAR can resolve echoes that are often interfered by surface clutter arising from rough surfaces like crevasses, moulins, etc. Hence, analysis of coherent radar echoes can better quantify reflection and scattering from an interface than incoherent radar analysis (Peters et al., 2005).

Basal melting is one of the necessary conditions for basal sliding and contributes to a higher ice surface velocity so understanding basal conditions is crucial for modeling ice dynamics (van der Veen et al., 2013). Bed echo reflectivity has been frequently used to infer the basal conditions (Peter et al., 2005; Oswald and Gogineni, 2008; Jordan et al., 2016; Chu et al., 2018) given that wet beds have higher reflectivity than frozen beds. But due to variable spatial attenuation dry beds are sometimes interpreted as wet beds. High specularity (Young et al., 2016), smooth bed and high waveform abruptness (Oswald and Gogineni, 2012) have also been used along with bed reflectivity to constrain the locations of wet beds.

This thesis studies the basal conditions of two important outlet glaciers of Greenland i.e. Jakobshavn and Petermann glacier which are rapidly changing outlet glacier in Greenland draining a lot of ice sheet into the ocean. The radar data collected by Center for Remote Sensing of Ice sheets during Operation IceBridge missions have been used to derive the basal conditions of these two glaciers. Here the roughness of ice surfaces and ice beds of the glaciers have been estimated using Grima's Radar Statistical Reconnaissance (RSR) method (Grima et al., 2012, 2014). Similarly, constant and variable attenuation models (Schroeder et al., 2016) have been used to estimate the englacial attenuation. Finally ice bed reflectivity maps have been generated by estimating reflectivity after compensating for geometric loss, rough interfaces and englacial

attenuation. This work helps to better understand the subglacial conditions of these two important glaciers.

1.2 Thesis organization

The thesis is organized as follows:

Chapter 2 describes the general theory and methodology used to derive the basal conditions. Firstly, it presents an overview of radar equations used for deriving ice bed reflectivity. Secondly, it introduces methods for roughness estimation of ice surface and bed. Thirdly, it discusses methods of englacial attenuation calculation including ice internal layer method, constant attenuation and variable attenuation models. It finally discusses ice basal conditions in terms of reflectivity values, as well as the concepts of abruptive and coherence indexes.

Chapter 3 reviews the study areas of Jakobshavn glacier and Petermann glacier, and describes the data sets used to infer the basal conditions of the study areas, the instruments used to collect the data sets, and the data processing methodology.

Chapter 4 presents the results of roughness, ice attenuation and bed reflectivity of the studied areas, including comparisons between roughness estimates from MCoRDS, ATM and Ku-Band measurements, the ice bed reflectivity maps, crossover analysis and the validation with bed topography, surface velocity and with previous results.

Chapter 5 is the summary and conclusions of this study. Future works that can improve the results of this study have also been presented.

Chapter 2 Theory and Methodology

2.1 Radar Equations

Airborne ice penetrating radars have been used to map subglacial and englacial interfaces of the ice sheet for a long time. The basic principle of an ice penetrating radar is that electromagnetic waves are transmitted through array of transmit antennas into the ice sheets where it is backscattered whenever there is discontinuity of dielectric constant thus giving sharp backscattered echoes from the surface, internal layers and the bottom as there is transition from air to ice and ice to rock/water. The receive antenna different from transmit antenna or the same antenna is used to capture the backscattered echoes. The data used in this study is collected by a multichannel coherent radar depth sounder (MCoRDS) which uses array of antennas for better SNR of the received echoes and the beamforming. It uses pulse compression in fast time and along track focusing by SAR processing to generate echograms usually for every 50 km. The two-way travel time for the surface and bed are then used to determine the depth of the ice sheets. Ice Surface and bottom are tracked using automatic tracker developed at CReSIS with some manual corrections. The detailed description of the radar system and data processing is given by Gogineni et al. (2001).

Figure 2.1 shows an echogram (left) that shows ice surface, internal layers and the ice bed (at 3100 m) clearly. The A-scope shows two distinct peak powers at ice surface and the ice bed. This ice bed can be rock of different dielectric constants, 4-12 or could be water of dielectric constant 80. The backscattered echo strength depends on the dielectric constant hence it may indicate water (wet bed) for higher reflectivity and rock for lower reflectivity (frozen bed).

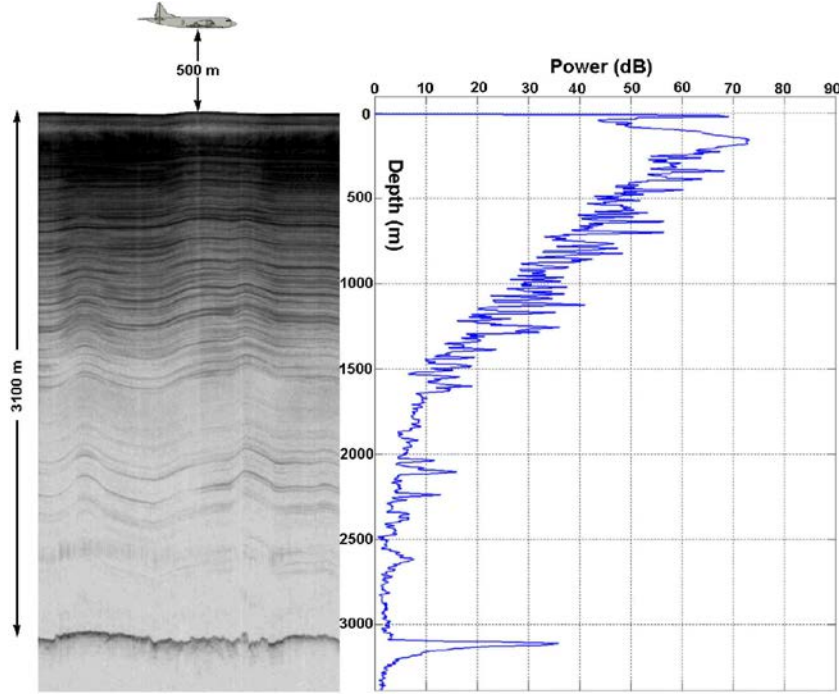


Figure 2.1 Radar Echogram (left), A-scope with received signal power versus depth (right) (Allen, 2008)

The signal power received ‘ P_r ’ by the radar from ice sheet with small scale roughness is given by (Gudmandsen, 1971; Sasha et al., 2008)

$$P_r = P_t \left(\frac{\lambda}{4\pi} \right)^2 \frac{G_t G_r}{[2(h + \frac{z}{n_i})]^2 L_i^2} \rho | < R_b > |^2 \quad (2.1)$$

where λ is the wavelength in air, G_t and G_r are the gains of transmit and receive antennas, ρ accounts for small scale roughness scattering effects, P_t is the transmitted power, h is the height of aircraft above ice, z is Ice thickness, n_i is index of refraction for ice, L_i is englacial attenuation, and $\langle R_b \rangle$ is the averaged basal reflection coefficient over the imaged resolution cell, given by

$$R_b = \frac{\sqrt{\varepsilon_1} - \sqrt{\varepsilon_2}}{\sqrt{\varepsilon_1} + \sqrt{\varepsilon_2}} \quad (2.2)$$

where ε_1 and ε_2 are complex dielectric permittivity of two media expressed as $\varepsilon = \varepsilon_r(1 - j \tan\delta)$, ε_r is the relative permittivity and $\tan\delta$ is the loss tangent.

The power reduction ρ is due to the phase change ϕ through the rough surface σ_h and can be calculated as (Schroeder et al., 2016)

$$\rho = e^{-\phi^2} I_0^2\left(\frac{\phi^2}{2}\right) \quad (2.3)$$

where I_0 is the zeroth-order modified Bessel function of the first kind and the phase shift ϕ is the is given by

$$\phi = \frac{4\pi\sigma_h}{\lambda} \quad (2.4)$$

If z is the total depth of ice sheet, then P_r gives the total power received from the ice bed. The radar equation can be written in dB as:

$$[P]_{dB} = [S]_{dB} - [G]_{dB} + [R]_{dB} - [L]_{dB} \quad (2.5)$$

where bed echo strength (P) is a function of radar system parameters (S), geometric spreading loss (G), bed reflectivity (R) and englacial attenuation (L). So to calculate the reflectivity 'R' of the bed we need to compensate all the other parameters from the bed echo strength 'P'. This bed reflectivity can then be used to analyze whether the bed is frozen or thawed (Dowdeswell and Evans, 2004; Oswald and Gogineni, 2008). When the signal is radiated from the antenna then the power of the signal is continuously reduced when it travels away from the antenna. The geometric loss at ice depth 'd' when radiated from an antenna at the height of 'h' is given by

$$G = 2 \times \left[2 \left(h + \frac{d}{\sqrt{\varepsilon}} \right) \right]_{dB} \quad (2.6)$$

Using the two-way propagation time of ice surface and ice bed, the depth of ice sheet is calculated from which the corresponding geometrical spreading loss is derived.

Geometrically corrected bed-echo power P_c is then given by

$$[P]_{dB} + [G]_{dB} = [P_c]_{dB} = [S]_{dB} + R_{dB} - [L]_{dB} \quad (2.7)$$

Rearranging the above Eq. (2.7) gives

$$R_{dB} = [P_c]_{dB} + [L]_{dB} - [S]_{dB} \quad (2.8)$$

Assuming the system is stable for a season and the losses due to birefringence negligible (<2 dB) (Fujita et al., 2006), then ice bed reflectivity is calculated by correcting the ice bed power for geometric losses, ice attenuation and system parameters as shown by Eq. (2.8). In addition, roughness correction is also done for losses due to rough interface (discussed in Chapter 2.2). Finally, the obtained ice bed reflectivity can be analyzed to infer basal conditions.

2.2 Roughness Estimation

Radar has been extensively used to understand the surface properties from determining elevation changes (Helm et al., 2014), surface roughness (Neal, 1982; Grima et al., 2014), moisture content (Rahaman et al., 2007; Zribi et al., 2002), dielectric constant (Grima et al., 2012) and so on. Studies using echo fading and amplitude statistics have provided estimates of small-scale roughness or the localized slope distributions of reflecting facets (Oswald, 1975; Neal, 1982). The changes of the ice sheet conditions are being monitored by flying missions over the same place in certain time period. One of the changes that can be identified is the change in the surface roughness that can show the changing nature of ice dynamics at that place.

Roughness can be estimated from radio echo sounding (RES) data using different methods like Fast Fourier transforms (Taylor et al., 2004), Integral Equation Model (Fung and Chen, 2004)

and statistical method (Grima, 2014). The MCoRDS radar used by the Center for Remote Sensing of Ice sheets (CReSIS) for polar surveys can penetrate deep into ice sheets to reveal ice bottoms and the backscattered signal from the bed (Rodriguez et al., 2014; Leuschen et al., 2016). These bed echoes are analyzed to understand the basal conditions (Oswald, 2008; Malyala et al., 2017). We apply Grima's approach to derive roughness of the ice bed and ice surface from MCoRDS data, which can be used to model ice bed reflectivity and understand basal conditions.

Roughness is a function of the radar system parameters as it varies with the wavelength of the radar signal. Roughness calculated by the MCoRDS (Rodriguez et al., 2014) is compared with that of laser altimeter by ATM group (Studinger, 2014) and Ku Band altimeter (Gogineni et al., 2015). However, RMS height is an inherent property of the system parameters (Baghdadi et al., 2002), and hence these systems are expected to have quantitatively different results but qualitatively similar results, which gives us confidence towards the calculation of ice bed reflectivity. Laser altimeter and Ku-band only map the ice surface, hence here we compare the surface RMS heights calculated from these three systems.

2.2.1 Roughness Estimation from MCoRDS measurements using Radar Statistical Reconnaissance Method (RSR)

Natural surfaces can reflect the EM waves according to the nature of the surface. From specular surfaces the received field is coherent with known phase given by $E = A e^{j\alpha}$ whereas from the rough surfaces they are scattered with unknown phase called the incoherent components. Both the

coherent and incoherent components contribute to the total signal received at the radar receiver which can be written as (Grima et al., 2014):

$$E = e^{j\varphi_0} + \sum_{i=1}^N A e^{j\varphi_i} \quad (2.9)$$

where the first part is the coherent component and the second part is the incoherent component of the power received at the radar receiver. The balance between these two is the function of surface roughness. If the surface is perfectly smooth, then it will have only coherent component or specular reflection i.e. only the first term. If the surface is made of N random scatters with increasing roughness, then the incoherent component would be dominant and the coherent component would become negligible. The instrument able to measure the coherent component is called a reflectometer and the one able to measure the incoherent term is called a scatterometer. However, a radar can be used as both and we can separate and estimate these two terms and relate it to the surface roughness.

In the specular direction, the coherent and incoherent component is given by (Ulaby et. al, 1986) as:

$$P_c = r^2 e^{-(2k\sigma_h)^2} \quad (2.10)$$

$$P_n = \frac{1}{\pi h^2} \iint_{A_0} \sigma^0 ds \quad (2.11)$$

Where $k = \frac{2\pi}{\lambda}$ is the wave number, A_0 is the footprint area, $r = \frac{1-\sqrt{\epsilon}}{1+\sqrt{\epsilon}}$ is the surface Fresnel coefficient, ϵ is the dielectric constant of first 6-8 m of ice sheet and σ^0 is the back scattering coefficient. Here the small perturbation model (SPM) is used since the phase difference induced

by the surface is less than 2π and its domain of validity is that the RMS height is within 5 % of the wavelength of the radar and this method is numerically easy to implement.

The backscattering coefficient derived from SPM for a Gaussian correlated surface is given by (Grima et al., 2012)

$$\sigma^0 = 4k^4 r^2 \sigma_h^2 l^2 e^{-(kl \sin \theta)^2} \quad (2.12)$$

where θ is the angle from the scatterer to the antenna surface normal. Using small angle approximation (SAA) so that $\cos \theta \approx 1$ and $\sin \theta \approx \frac{||r_0||}{h}$, where $||r_0|| = \sqrt{r_x^2 + r_y^2}$ is the norm of the scatterer position vector in the surface plane where the origin is the intersection with the antenna surface normal, and substituting Eq. (2.12) in Eq. (2.11) we get

$$P_n = \frac{4}{\pi h^2} k^4 r^2 \sigma_h^2 l^2 \int_{-\frac{X}{2}}^{\frac{X}{2}} \int_{-\frac{Y}{2}}^{\frac{Y}{2}} e^{-(r_x^2 + r_y^2)(kl/h)^2} dx dy \quad (2.13)$$

where P_n is integrated over the rectangular footprint with lengths ‘X’ and ‘Y’. The double integral can be linearly solved to get the relation where erf (.) is the error function as

$$P_n = 4k^2 r^2 \sigma_h^2 \text{erf}\left(\frac{kl_x X}{2h}\right) \text{erf}\left(\frac{kl_y Y}{2h}\right) \quad (2.14)$$

where the correlation length is split into two parts l_x and l_y for the integration purposes.

The radar footprint is bounded by across track with length D_{PL} and along track by length D_X given by (Grima et al., 2014):

$$D_{PL} = 2 \sqrt{\frac{hc}{\Delta f}} \quad (2.15)$$

$$D_X = \frac{\lambda h}{2L} \quad (2.16)$$

where h is the range to the surface and Δf is the bandwidth and L is the synthetic aperture length.

Substituting the Eq. (2.15) and Eq. (2.16) in Eq. (2.14) we get,

$$P_n = 4k^2 r^2 \sigma_h^2 \operatorname{erf}\left(\frac{\pi l_x}{2L}\right) \operatorname{erf}\left(k l_y \sqrt{\frac{c}{h \Delta f}}\right) \quad (2.17)$$

Dividing Eq. (2.10) by Eq. (2.17), we get the power ratio independent of Fresnel coefficient and determined only by the roughness characteristics of surface as

$$\frac{P_c}{P_n} = e^{-(2k\sigma_h)^2} \cdot [4k^2 \sigma_h^2 \operatorname{erf}\left(\frac{\pi l_x}{2L}\right) \operatorname{erf}\left(k l_y \sqrt{\frac{c}{h \Delta f}}\right)]^{-1} \quad (2.18)$$

The error functions can be neglected if $l_x > 89m$ and $l_y > 0.36\sqrt{h}$ i.e. $l_y > 8 - 16m$.

Here the processing to achieve better resolution makes the equation sensitive to correlation length.

Neglecting the error functions, Eq. (2.18) can be rewritten as:

$$\frac{P_c}{P_n} = \frac{e^{-(2k\sigma_h)^2}}{4k^2 \sigma_h^2} \quad (2.19)$$

The fitting of N echo amplitudes should be applied based on the nature of the surface or scatters. The fundamental H-K distribution is best used to explain the surfaces when at the limiting conditions and gives better results when explaining the natural surfaces on the earth but it does not have a closed form and cannot be solved without numerical tools. The Rician distribution can also be used to explain the ice surfaces except when the distribution is negative binomial distribution which generally is not the case for ice surfaces. The Rician distribution is given by (Grima et al., 2012)

$$P(A|a, s) = \frac{A}{s^2} e^{-\frac{A^2 + a^2}{2s^2}} I_0\left(\frac{aA}{s^2}\right) \quad (2.20)$$

for interval $[a, \infty]$, where $I_0(z)$ is the modified Bessel function of first kind with zero order and ‘a’ and ‘s’ are the shape parameters. From the Rician fitting, the coherent and incoherent power can be obtained as (Grima et al., 2012):

$$P_c = a^2 \quad (2.21)$$

$$P_n = 2 s^2 \quad (2.22)$$

Coherent power ‘ P_c ’ and incoherent power ‘ P_n ’ derived from the statistical power distribution fitting are used in Eq. (2.19) to derive the RMS height σ_h for the radar.

2.2.2 Roughness Estimation from ATM Measurements

In addition to the roughness calculations from MCoRDS measurements, ATM has also supplemented these calculations. Airborne Topographic Mapper (ATM), an airborne laser altimeter, measures the surface elevation based on the two-way travel time of laser pulses along with the differential GPS and aircraft attitude information. The along-track resolution spacing is usually 3-4 m with laser footprint of ~1m. The primary data product of ATM is QFIT, which is dense surface elevation measurements (Brock et al., 2002). A QFIT file is a collection of geolocated laser shots tagged with time and elevation. It is condensed and resampled into ICESSN which fits a plane to the block of points selected at regular intervals (0.5 sec) along track with overlapping of 50% between successive blocks (Studinger, 2014). The radar lines of MCoRDS coincide with the track 0 of ICESSN data. ICESSN data has along-track resolution of 80 meters and hence the RMS height from this laser system is calculated by the interpolation at the corresponding radar locations.

2.2.3 Roughness Estimation from Ku band Altimeter Measurements

Apart from these two systems, the surface elevation measurements from Ku-band altimeter is also used to derive the roughness of ice surface. The along-track resolution interval of the data from the Ku- band altimeter is about 0.2 meters with about 2.5 cm range resolution in ice (Gomez-Garcia et al., 2012). RMS height is calculated using ice surface elevation measurements within along-track distance of every 200 m with 50% overlapping as:

$$\sigma_h = \sqrt{\frac{1}{N} \sum_{i=1}^N (z_i - \bar{z}_i)^2} \quad (2.23)$$

Where σ_h is the RMS height, z_i is the ice surface elevation for N samples within the sampled space and \bar{z}_i is the mean ice surface elevation within the sampled space.

The power loss ' ρ ' due to rough surface ' σ_h ' is due to the phase variation \emptyset which is given by (Schroeder et al., 2016).

$$\emptyset = \frac{4\pi \sigma_h}{\lambda} \quad (2.24)$$

$$\rho = e^{-\emptyset^2} I_0^2\left(\frac{\emptyset^2}{2}\right) \quad (2.25)$$

2.3 Englacial Attenuation Estimation

When electromagnetic waves travel through a medium then it is attenuated in the medium due to different phenomena like scattering, absorption, etc. Depending upon the medium the rate of attenuation varies. Similarly, in ice mapping there is attenuation of signal varying on ice constituents, ice depth, and internal structures and so on. Hence there is no constant attenuation of the signal through ice and needs to be properly compensated depending on the location. This uncertainty in radar attenuation can lead to uncertainty in basal reflectivity.

Usually ice attenuation is measured in terms of depth where englacial attenuation loss is given by

$$L = 2N_a d \quad (2.26)$$

where L is englacial attenuation loss in dB, N_a is one way depth averaged attenuation rate(dB/km) and d is the depth of ice bed.

Ice core data have been used to determine the englacial attenuation in lab environments but due to spatial variability, it cannot be used over a large area. Hence different methods have been used to derive the englacial attenuation rate where it is data dependent.

2.3.1 Layer Method

This method is used to calculate the englacial attenuation due to ice by tracing the power reduction through the specular ice internal layers.

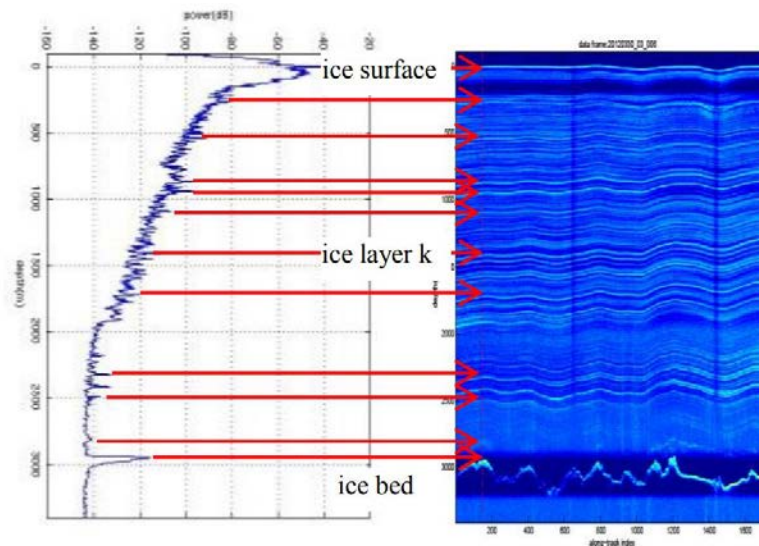


Figure 2.2 Echogram with tracking of specular layers (Li, 2014)

Radar echogram having distinct internal layers are traced and the power reduction through ice versus depth is plotted to fit an englacial attenuation value and calculate total ice loss at the ice bed by extrapolation (Li, 2014).

From each specular internal layers, the power loss from the surface is calculated and then it is fit to extrapolate the total ice attenuation at the ice bed.

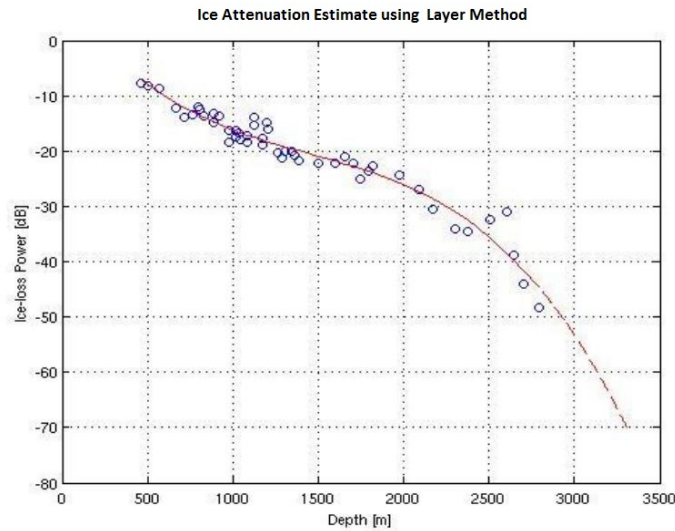


Figure 2.3 Ice Attenuation Estimate using Layer Method (Li, 2014)

As shown in Fig. 2.3, the total ice attenuation at ice bed of depth 3316 meters is -70.5 dB which can be used to compensate for the ice loss to calculate the ice bed reflectivity. However, this method is not applicable for the whole survey area because not all internal layers are visible as shown in the figure and neither are they accurately traceable from the echograms.

2.3.2 Constant Attenuation Model

Constant attenuation model assumes that the power varies linearly with depth. In this model, a constant attenuation value is used for the whole dataset where it is derived by fitting the

geometrically corrected bed power against depth. It can only be applied to a small area where the attenuation does not vary much.

As discussed in Chapter 4, the ice bed power after geometric correction gives

$$[P_c]_{dB} = [S]_{dB} + [R]_{dB} - [L]_{dB} \quad (2.27)$$

If we assume that the settings of the radar were not changed during the data recording, then the relative geometrically corrected power is given by

$$[P_r^c]_{dB} = [P_c - \bar{P}_c]_{dB} = [R - \bar{R}]_{dB} = [L - \bar{L}]_{dB} \quad (2.28)$$

$$[L - \bar{L}]_{dB} = 2 N_a (d - \bar{d}) \quad (2.29)$$

where \bar{d} is the mean ice depth.

There are two unknowns in Eq. (2.28), ice bed reflectivity and ice attenuation. Assuming reflectivity to be constant enables us to calculate ice attenuation by fitting the equation as:

$$-[P_r^c]_{dB} = 2 N_a (d - \bar{d}) \quad (2.30)$$

Here the term is $-P_r^c$ is termed as apparent attenuation and will help in modeling the constant ice attenuation rate ' N_a '. Then following Eq. (2.28) and (2.29), ice bed reflectivity can be estimated. These relative reflectivity values can then be used to estimate the basal conditions with higher reflectivity value associated with basal melting (Dowdeswell and Evans, 2004; Oswald, 2008).

This constant attenuation rate, however, is not physically realistic since it ranges over the values for potential subglacial materials (Peters et al., 2005). Calculation of proper attenuation rate is necessary because it can change the reflectivity values and may lead to false results. Hence a better englacial attenuation model is necessary which also considers the spatial variability of englacial attenuation rather than constant attenuation model.

2.3.3 Variable Attenuation Model

Variable attenuation model uses the constant attenuation derived from the overall data as initial estimate of the englacial attenuation and calculates the local variability in the attenuation rate. It is usually used for the radar lines extending from a higher depth towards shallower region so as to use the along track derivative of attenuation rate (Schroeder et al., 2016) for local scatter based fitting for better attenuation rate calculation (Schroeder et al., 2016).

$$N_a = \overline{N_a} + \frac{\partial N_a}{\partial x} (x - \bar{x}) \quad (2.31)$$

Here first the constant attenuation rate $\overline{N_a}$ for the whole area is calculated by fitting filtered geometrically corrected ice bed power versus depth.

$$[P_r^c]_{l1} = -2 \overline{N_a} \{d - \bar{d}\}_{l1} \quad (2.32)$$

It is filtered with a longer filter usually of several ice thicknesses like 30 km so as to capture the overall trend of the survey area. After that $\frac{\partial N_a}{\partial x}$ is calculated by fitting P_r^c in Eq. (2.33) for each survey line where the shorter filter $l2$ is comparable to horizontal scale of significance to preserve local variations.

$$[P_r^c]_{l2} = -2 \frac{\partial N_a}{\partial x} (x - \bar{x}) (d - \bar{d})_{l2} - 2 \overline{N_a} \{d - \bar{d}\}_{l2} \quad (2.33)$$

The improved relative reflectivity then can be calculated as

$$[R_r]_{dB} = [P_r^c]_{dB} + 2 \left(\frac{\partial N_a}{\partial x} \right) (x - \bar{x}) \{d - \bar{d}\}_{l2} + 2 \overline{N_a} \{d - \bar{d}\}_{l2} \quad (2.34)$$

With variable attenuation model, the local scatter based fitting helps in preserving the trend within each radar lines. Here variable attenuation model has been applied to the dataset to compensate for the total ice attenuation loss.

2.4 Ice bed Reflectivity and Basal Conditions

2.4.1 Interpretation of Basal Conditions

As discussed earlier, ice bed reflectivity after compensating for geometric losses, ice attenuation, rough surface compensation gives the properties of the ice bed. This resulting ice bed reflectivity is due to the properties of the ice bed like basal dielectric constant and bed roughness (Peters et al., 2005). A transition from frozen to wet bed would correspond to ice bed reflectivity increase in about 10 dB (Macgregor et al., 2013).

The reflectivity due to dielectric constant difference can be shown as (Allen, 2018):

$$\Gamma = |R|^2 = \left| \frac{\eta_2 - \eta_1}{\eta_2 + \eta_1} \right|^2 \quad (2.35)$$

$$\Gamma = \left| \frac{\sqrt{\epsilon_1} - \sqrt{\epsilon_2}}{\sqrt{\epsilon_1} + \sqrt{\epsilon_2}} \right|^2 = \left| \frac{1 - \sqrt{\epsilon_2/\epsilon_1}}{1 + \sqrt{\epsilon_2/\epsilon_1}} \right|^2 \quad \text{for } \theta = 0^\circ \quad (2.36)$$

$$\Gamma_{air/ice} = \left| \frac{1 - \sqrt{3.2}}{1 + \sqrt{3.2}} \right|^2 = (-0.283)^2 = 0.08 = -11 \text{ dB}$$

$$\Gamma_{ice/rock} = \left| \frac{1 - \sqrt{1.88}}{1 + \sqrt{1.88}} \right|^2 = (-0.156)^2 = 0.024 = -16 \text{ dB}$$

$$\Gamma_{ice/water} = \left| \frac{1 - \sqrt{25.3}}{1 + \sqrt{25.3}} \right|^2 = (-0.668)^2 = 0.447 = -3.5 \text{ dB}$$

Here we can see that the reflectivity would be higher for ice water interface compared to ice rock interface due to difference in dielectric constant. Hence a higher reflectivity would be representative of basal melting if proper compensation of losses is done. Apart from ice bed

reflectivity several other properties of the beds such as abruptive index and coherence index can be used to constrain the basal melting.

2.4.2 Abruptive Index

Oswald and Gogineni, 2008 have used high abruptness as another indicator of basal melt since the transition from ice to flat lying water bed gives a specular echo. Abruptive index is defined as:

$$I_{abr} = \frac{P_{peak}}{P_{ag}(x)} = \frac{(\{P\}_X)_{peak}}{\{\sum D_{int} P\}_X} \quad (2.37)$$

where P_{peak} is the bed power and $P_{ag}(x)$ is the aggregate power over the echo envelope D_{int} which is the depth bins and is given a threshold of 5% of the peak power. Its value lies usually between 0.05 and 0.5. A threshold value of abruptive index is put upon the interface that is flat at the scale of ice depth to indicate possible basal melt.

2.4.3 Coherence Index

To measure the interface smoothness, the coherence index of the bed needs to be calculated which is given by equation:

$$I_{CO} = \frac{\int_{D_{int}} <|\int_{X_{int}} |\psi(D,x)dx|^2 > dD}{\int_{D_{int}} \int_{X_{int}} |\psi(D,x)|^2 dx dD} \quad (2.38)$$

where D is the ice depth, x is the along track distance interval for integration, and X_{int} is the along track interval for both coherent and incoherent integrations, the length of the radar footprint at ice bed, usually 200 meters, and D_{int} is the aggregation interval of the basal echo envelope.

If there is water at the bed then due to pressure gradient it forms a flat surface hence the areas with flatter surfaces and high coherence index are often representative of basal melt (Oswald and Gogineni, 2008).

Chapter 3 Study Areas and Data

3.1 Petermann Glacier

Petermann glacier is one of the rapidly changing outlet glaciers in Northern Greenland that drains more than 4% of the total Greenland ice sheet and discharges nearly 12 Gt/yr of ice (Rignot and Steffen, 2008). The glacier is situated around 81°N and 61°W and flows from south-east to north-west as shown in Figure 3.1.

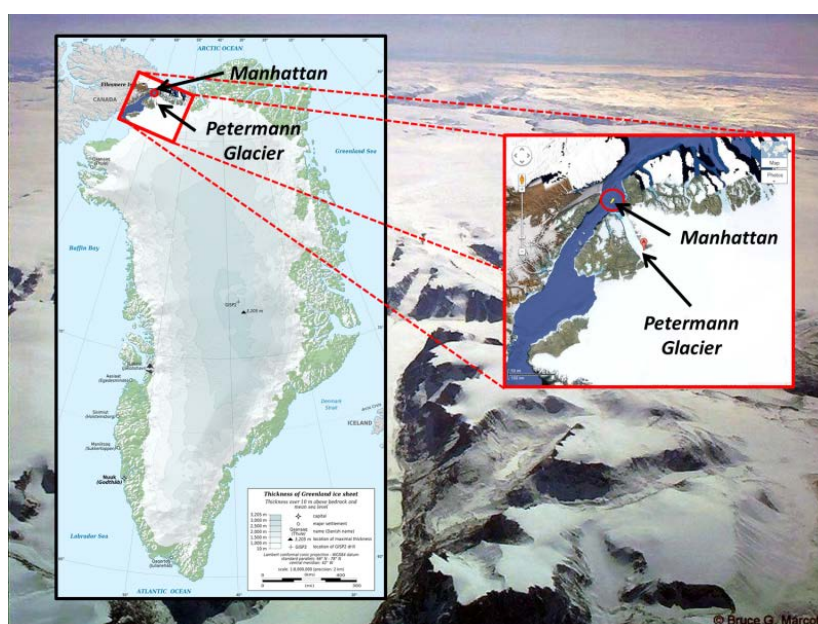


Figure 3.1 Petermann glacier (Middleton, 2012)

The 90 km long fjord has the deepest bed up to 1100m below the sea level. The ice tongue thins from nearly 600m thickness at the fjord front to around 100m at glacier front (Munchow et al., 2014) with ice thinning caused due to melting of underside ice by warm ocean water (Rignot and Steffen, 2008].

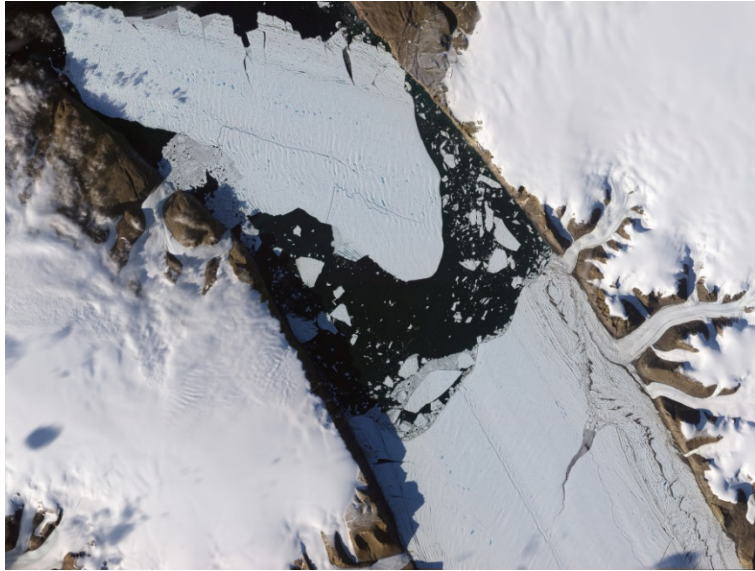


Figure 3.2 Petermann glacier ice tongue (Middleton, 2012)

Petermann glacier has the second-longest floating ice shelf in Greenland with a permanent floating ice tongue as shown in Figure 3.2 (Rignot et al., 2001; Moon et al., 2007) and flows with an average velocity of just over 1 km per annum (Nick et al., 2012).

Two huge glacier calving events have occurred at Petermann Glacier over the past 5 years, one in 2010 (270 km²) and another in 2012 (130 km²) (Falkner et al., 2011; Nick et al., 2012). The findings of Nick et al. (2012) and Macdonald et al. (2018), show that the subglacial melting plays a critical role in the dynamics of Petermann Glacier, and understanding it can help predict future calving events.

3.2 Jakobshavn Glacier

Jakobshavn glacier is in South West Greenland, the fastest moving glacier on earth which has very high ice calving rate. It now flows approximately at 1250m^{yr}⁻¹ and drains nearly 7% of the total ice sheet (Bindshadler, 1984) through 50 km long fjord to a bay. It forms at the confluence of two ice streams, a short slow one from the north and a long fast one from the east (Fastook et al., 1995).

Much of the floating tongue of Jakobshavn isbrae has collapsed resulting into the accelerating of the glacier. This may be due to warming of the ocean water causing sub ice shelf melting or the subglacial drainage system in the catchment area.

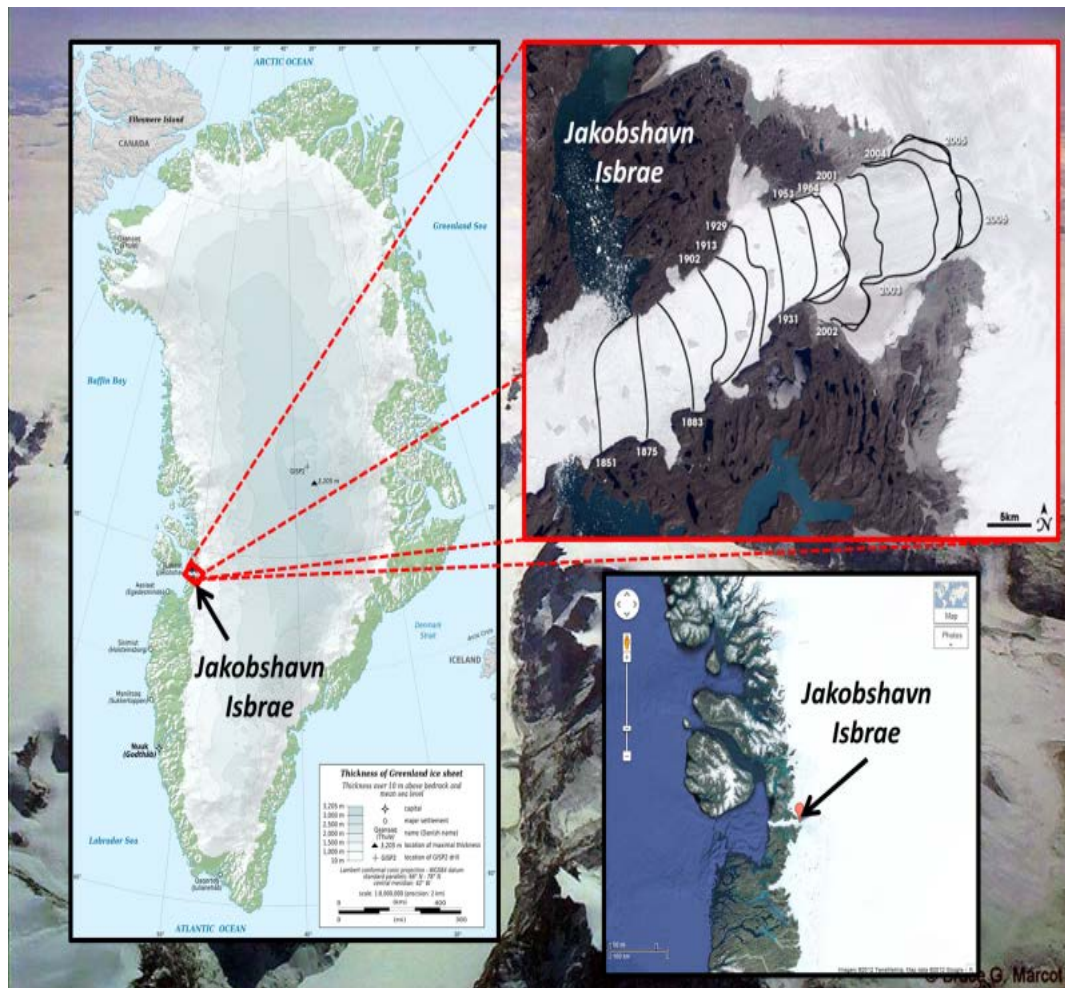


Figure 3.3 Jakobshavn glacier (Middleton, 2012)

The glacier's high flow acceleration and mass loss in addition to ice calvings have become major concerns for the stability of this glacier. A recent large calving on August, 2015 showed largest calving in Jakobshavn till date with an area of 12.5 km^3 (Harvey, 2015). Understanding the ice dynamics of this glacier is thus very important to predict its response in coming years.

3.3 Radar Systems and Data

3.3.1 MCoRDS

The Center for Remote Sensing of Ice Sheets (CReSIS) deployed airborne Multi Channel Coherent Radar Depth Sounder (MCoRDS), a nadir looking radar mounted on an aircraft flying usually at the height of 500 meters from the ice surface to map the thickness of Greenland and Antarctica ice sheets in NASA's Operation Ice Bridge (OIB) missions (Rodriguez et al., 2014; Gogineni et al., 2015). This analysis uses the data at Petermann glacier and Jakobshavn glacier from 2008 to 2014 seasons (Leuschen et al., 2016).

MCoRDS system has evolved over the years and the specifications for each season can be obtained from CReSIS. MCoRDS operates with linear chirp waveform within the frequency band from 180 MHz to 210 MHz (2012 season). It usually has six transmit channels and receivers to allow beamforming during data processing. An Arbitrary waveform generator (AWG) is used to generate the waveforms which is pre-stored in digital form and converted to analog form using a D/A converter (Rodriguez et al., 2014). Three different pulses are used. The short pulses of 1 μ s and 3 μ s are used to detect the surface and shallow ice layers and do not have high penetration power whereas 10- μ s pulse is better in detecting the ice bed as it has higher penetration power. The short and long pulses are alternatively sent with time division multiplexing at pulse repetition frequency of 12 KHz. The received signals are digitized using A/D converters at a sampling rate of 111MHz or 150 MHz with 14 ADC bits. Table 1 describes some basic radar system parameters.

Table 1 MCoRDS System Parameters

Parameter Description	Value
Center Frequency	195 MHz
Bandwidth	180-210 MHz
Transmit Signal Type	Linear Up Chirp
Transmit Power	1050 W
Pulse Repetition Frequency	12 KHz
Signal Duration	1 μ s, 3 μ s and 10 μ s (Low Altitude) 30 μ s (High Altitude)
Transmit Channels	7
Receive Channels	15
Noise Figure	2
Sampling Rate	111/150 MHz
ADC Bits	14
Data Rate	32 MB/sec per channel

The complex data received after processing from this radar without coherent integrations has along track resolution of about 0.5 m and 25m when SAR processed. The resolution in ice is about 4.3 (Oswald and Gogineni, 2008). The surface illuminated by the radar or its footprint is important in deriving the surface roughness. For any radar, the footprint bounded by compressed pulse length is given by (Grima et al., 2014):

$$D_{PL} = 2 \sqrt{\frac{hc}{\Delta f}} \quad (3.1)$$

where ‘h’ is the height of the aircraft from the surface, Δf is the bandwidth of the radar signal. For MCoRDS, the flying height is typically 500 meters and the bandwidth being 30 MHz the radar

footprint thus averages around 141 meters for ice surface and for average ice depth of 2000 meters, the footprint is around 316 meters.

3.3.2 Airborne Topographic Mapper (ATM)

Airborne Topographic Mapper (ATM) is a conical scanning airborne laser developed at NASA Wallops Flight Facility to monitor the earth's topography. It measures topography to an accuracy of 10 centimeters (Kwok et al., 2012). It is used for change detection by flying over the same location after a certain time. ATM measures the surface elevations with a pulse repetition frequency of 5 kHz and a scan rate of 20 Hz (Kwok et al., 2012). The along-track resolution is 3-4 m with laser footprint of ~1m (Kwok et al., 2012).

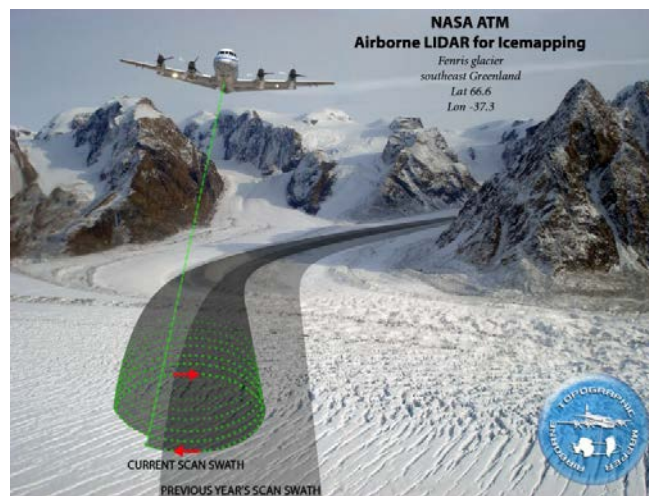


Figure 3.4 Airborne Topographic LIDAR (ATM) (NASA, 2009)

Fig. 3.4 shows NASA's Airborne Topographic Mapper (ATM) on an aircraft with conical scans. The primary data product LIB of ATM is QFIT, shown by green dots in Fig. 3.4. It is condensed into ICESSN which fits a plane to the block of points selected at regular intervals (0.5 sec) along track with overlapping of 50% between successive blocks (Studinger, 2014). It also

measures the South-North and West-East slope for the plane and RMS fit of the ATM data to the plane.

3.3.3 Ku Band Altimeter

Operation IceBridge missions also employ the Ku-band Altimeter developed by CReSIS which is an Ultra-Wideband Frequency (UWB) Modulated Continuous wave (FMCW) radar operating usually from 12-18 GHz (Rodriguez, 2014). It provides high precision surface elevation measurements over polar ice sheets along with shallow internal layers (Gomez-Garcia et al, 2012). The along-track resolution of the data from Ku- band is about 0.2 meters and the range resolution is about 2.5 cm (Gomez-Garcia et al, 2012). Some of the specifications of the system are listed in Table 2 (Gomez-Garcia et al., 2012).

Table 2 Ku band Altimeter Specifications

Parameters	Value
Center Frequency	15 GHz
Bandwidth	6 GHz
Chirp Length	250 μ s
Pulse Repetition Frequency	2 KHz
Transmit Power	16 dBm
Antenna Gain	20 dB
ADC Sampling Rate	62.5 MSPS
Range Resolution in Ice	2.5 cm

Chapter 4 Results and Discussions

4.1 Application of RSR

The particular segment 20141026_02 from Antarctica, as shown in the red line in Figure 4.1, is used to analyze the application of RSR on MCoRDS data because of the quality of data and DMS (Digital Mapping System) pictures. Figure 4.2a and Figure 4.2b show areas with a smooth surface and rougher surface respectively together with their corresponding Ku-band radar echograms in Figure 4.2c and Figure 4.2d, illustrating the variable surface roughness.

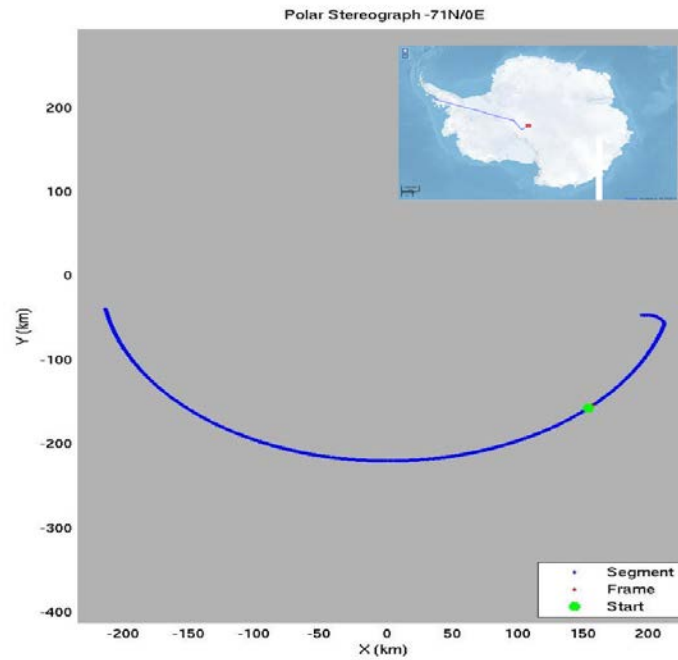


Figure 4.1 Area used for Roughness Comparison and Verification

Here the echo amplitudes of around 600 samples (i.e. about 200 m along track) are fit to the Rician distribution to derive the surface RMS height using MATLAB. To validate the RMS height derived from MCoRDS using Grima's method, the RMS height was also derived for the corresponding radar locations using laser data.

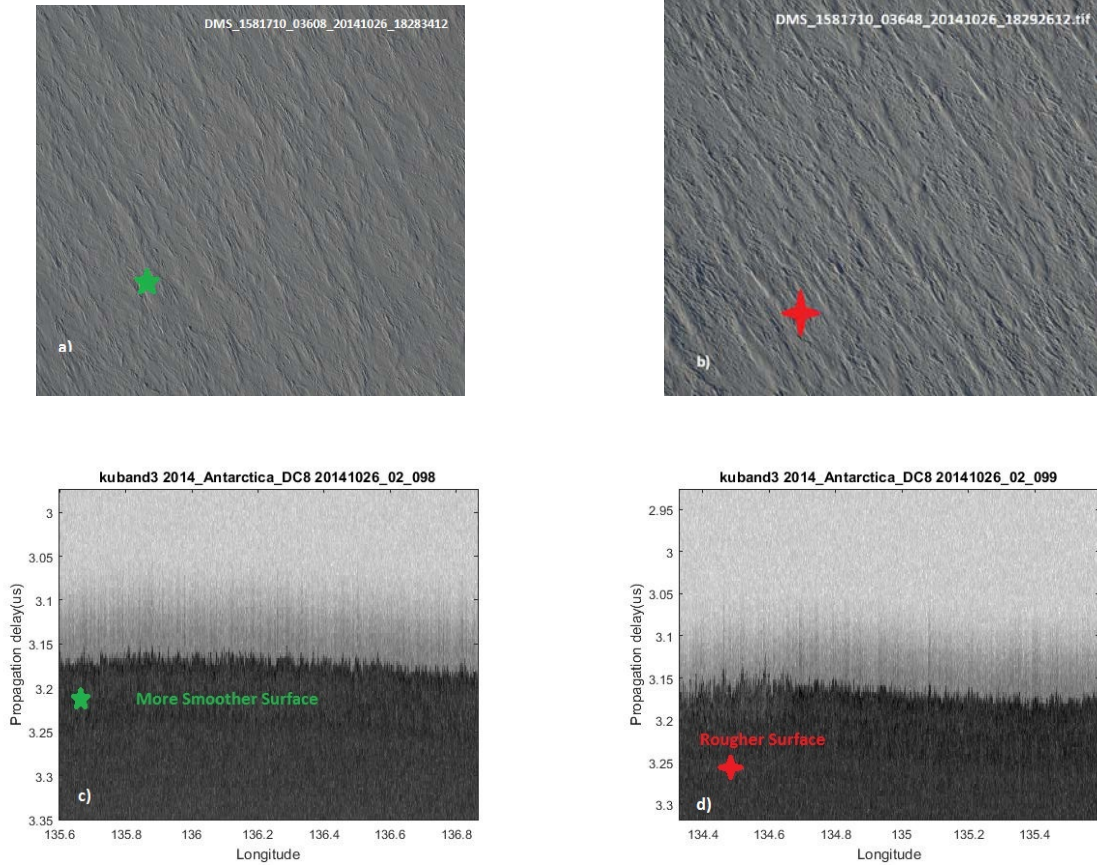


Figure 4.2 DMS pictures of areas with Smoother (a) and Rougher (b) Surfaces [29]. (c) and (d) Radar Echograms obtained from Ku-band altimeter showing corresponding smoother (a) and rougher areas (b)

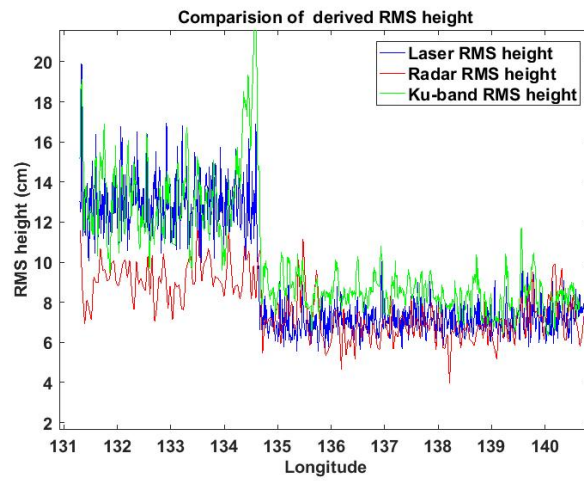


Figure 4.3 Surface RMS heights obtained from MCoRDS (red), ATM (blue) and Ku-band altimeter (green)

Figure 4.3 shows the comparison between the surface roughness measurements obtained from these three systems, red indicating radar, blue indicating laser and green indicating Ku-band measurements. It can be clearly observed that the RMS height calculated corresponds to the surface features seen in the Ku-Band altimeter image. The rougher surface features from the echogram coincide with the corresponding higher value of RMS height whereas same for the comparatively smoother surfaces of lower RMS value.

It can be distinguished that the areas with higher RMS in laser data are also seen rough by the radar however there is a certain bias which can be owed to the facts that these are two different systems operating with different system parameters and ground surface roughness being the inherent property of radar specifications (Baghdadi et al., 2002). The RMS heights detected by radar is bounded because this uses power statistics and signal components fade and become undetectable with increasing roughness (Grima et al., 2012, 2014). In addition to this, the data obtained by Ku-band altimeter of CReSIS analyzed for the corresponding frames yielded similar results.

Following this method, it was used to determine the surface and bed roughness of Peterman and Jakobshavn Glacier, which can be later used to model the ice bed reflectivity.

4.2 Peterman Glacier Basal Conditions

4.2.1 Roughness Estimate of Peterman Glacier

As shown in Fig. 4.4 (A), the longitudinal radar survey lines extend from inland towards the ice margin from southeast to northeast, and the cross lines extend from northeast to southwest. Straight lines are chosen as there is no loss due to aircraft banking.

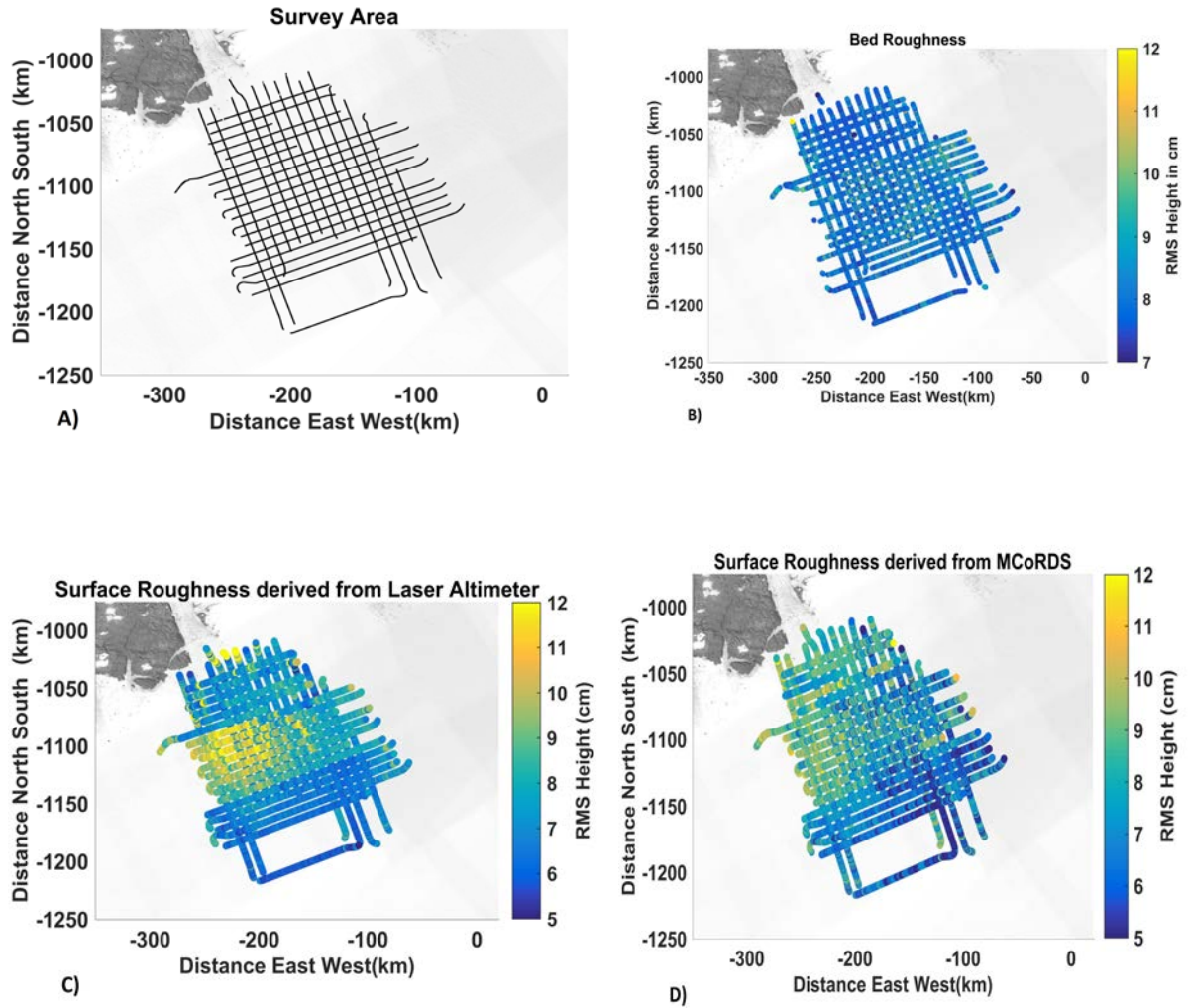


Figure 4.4 Radar Survey area of Petermann Glacier under Operation IceBridge (A), Bed Roughness calculated from MCoRDS (B), Surface Roughness calculated from MCoRDS (C), and Surface Roughness calculated from ATM (D).

The surface roughness for Peterman glacier obtained using radar data and laser data are shown in Figure 4.4 C and D. Ku-band data are not available for this complete dataset hence not presented, however, are cross-checked whenever available. Crossover analysis was done for obtained roughness which has 75% of the RMS height difference within ± 2 cm. The results reveal that the surface roughness is greater towards the coastline, which is expected since the ice flow is

obstructed at the coastline due to a narrow passage and also the presence of surface crevasses. As shown in Fig. 4.5, the areas with crevasses correspond to higher RMS height.

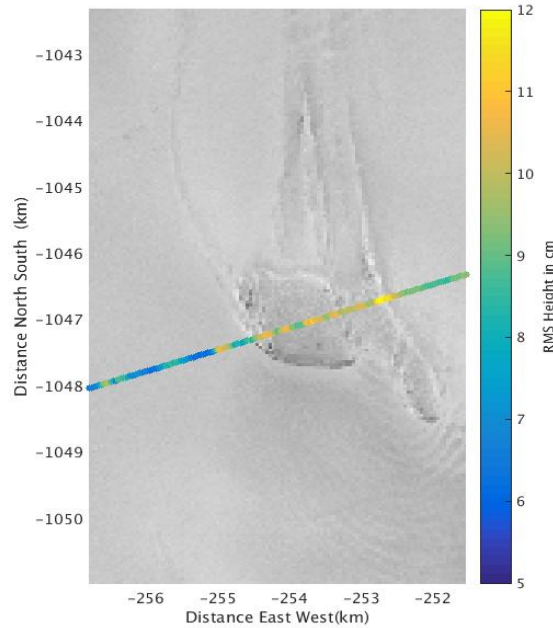


Figure 4.5 . Surface RMS Height at Crevasse as seen from LANDSAT Imagery (Rough Location)

Similarly, higher RMS height values are seen towards the Northwest area. The difference between the radar derived RMS heights and laser derived RMS heights is within ± 5 cm (99%) for the survey area. Fitting errors may be introduced when RMS height is fit into Eq. (2.19) so it should be checked for convergence. Some of the errors to this method may also result from the surface and bottom tracking errors but automatic surface tracking method employed here decreases this type of errors. Also when the slope of the surface and roll of the aircraft is large then surface power is decreased hence constraints are applied on the roll and slope to minimize such errors. Areas with very high surface elevation changes have been removed since the surface stationarity is not maintained.

In contrast, as shown in Fig. 4.4 (B) the bed roughness shows that the bed is relatively pretty smooth for Petermann Glacier with some rough areas towards eastern shear margin. Petermann Glacier lies in a deep subglacial trough, flanked by steep valley sides so it is fed by large area of ice sheet (Rippin, 2013). The flow rate is higher towards the margin of the glacier (Joughin et al., 2010). The smoother bed allows easier flow of ice sheets towards the ice margin.

4.2.2 Englacial Attenuation Estimation of Peterman Glacier

For Peterman data, data from 2010 and 2011 seasons were used to calculate the ice bed reflectivity map. The data were collected using MCoRDS with a center frequency of 195 MHz. However, there are some changes in the specifications of these radars used in two seasons (CReSIS) and hence the ice bed power from these two seasons have different dynamic ranges as shown in Fig. 4.6 and 4.7. One of the techniques would be to level these two seasons instead in this work, these two seasons have been separately processed with their individual mean values and attenuation rates.

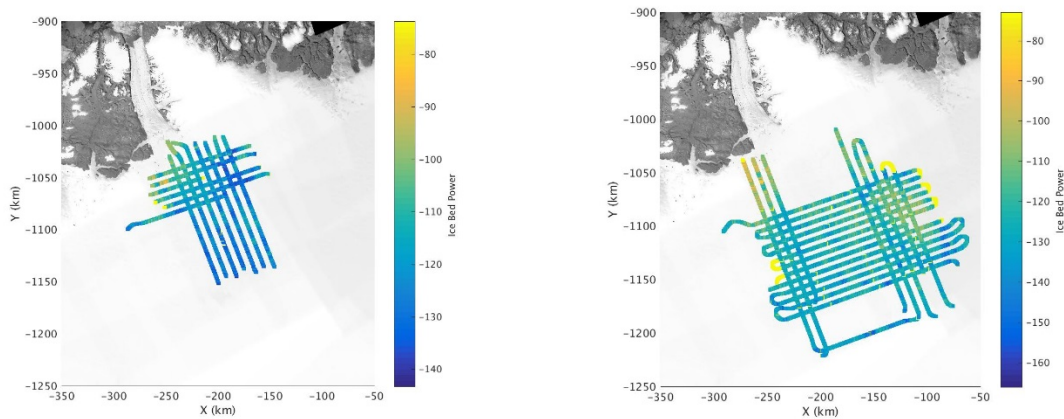


Figure 4.6 Ice Bed Power 2010 season (left) and 2011 season (right)

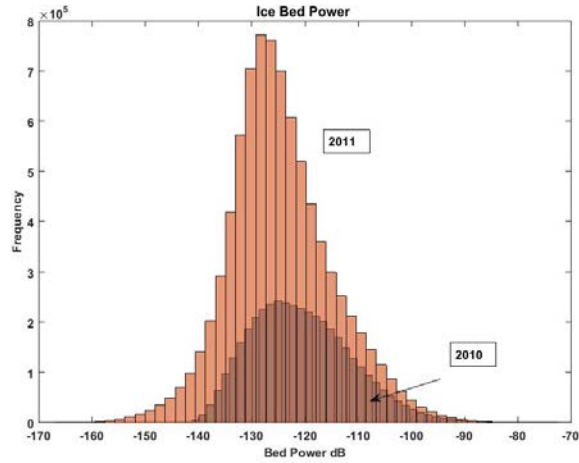


Figure 4.7 Histogram of Ice Bed Power for two seasons

The geometrically corrected power for these two seasons have the statistics as follows:

Table 3 Ice Bed Power Statistics

	2010 season	2011 season
Median (dB)	-53.6862	-56.4252
Mean (dB)	-42.563	-44.0918
Dynamic Range (dB)	65.9282	87.6254
Mean Depth (km)	1.3341	1.6612

To calculate the ice bed reflectivity at Peterman glacier, the bed power was derived by using CReSIS automatic tracker. The along-track resolution of the data is about 0.5m. The power is averaged for every 200m where the surface and bed roughness correction is also applied. The mean correction due to surface roughness is about 0.6861 dB with the highest value for rougher areas of 2.6156 dB shown in Fig. 4.8 (left). Similarly, for the bed power correction due to bed

roughness was also about 0.6334 dB with largest correction of 10.7824 dB at few rougher locations shown in Fig. 4.8 (right).

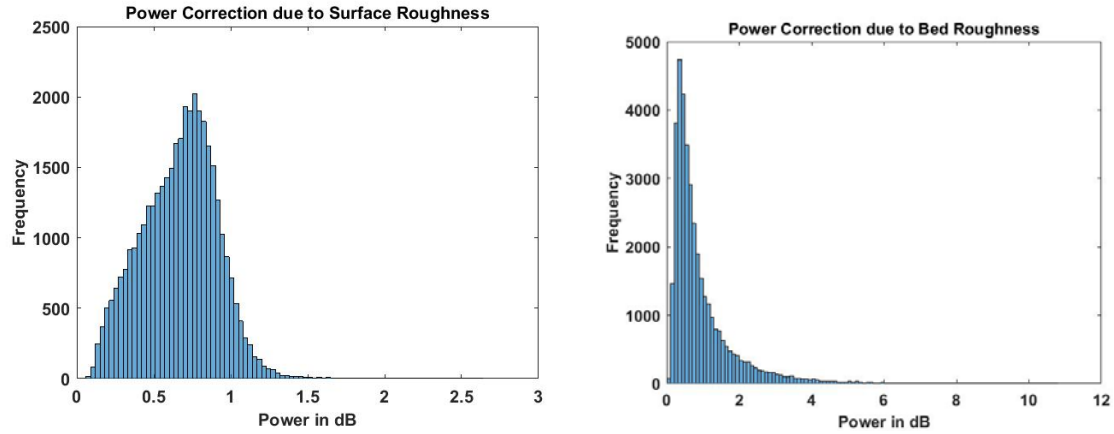


Figure 4.8 Power Correction due to Surface Roughness (Left) and due to Bed Roughness (Right)

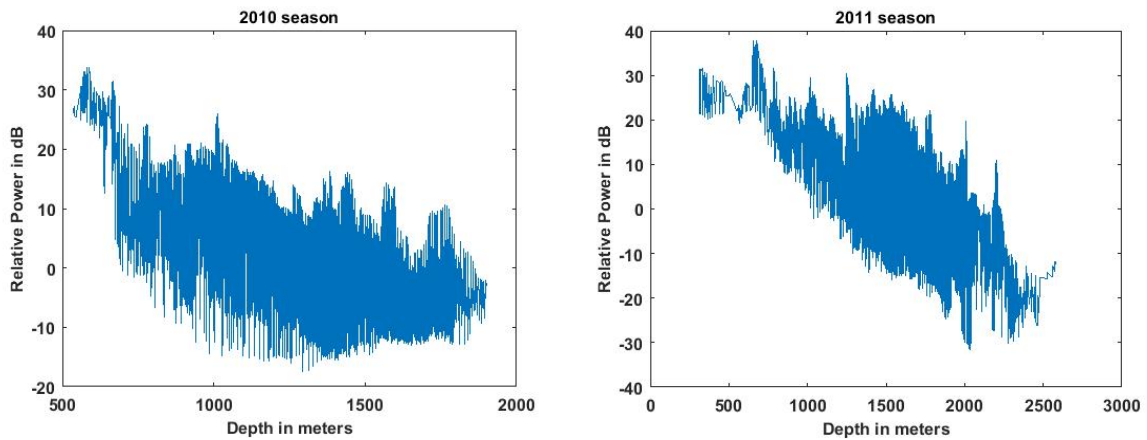


Figure 4.9 Geometrically corrected Relative Ice bed power for 2010 and 2011 season

To calculate the englacial attenuation for Peterman glacier, two seasons 2010 and 2011 having different system parameters thus different mean ice bed power have been geometrically corrected after correcting for rough interfaces shown in Fig. 4.9 and using regression, the depth-

averaged attenuation rate for two seasons $\overline{N_a}$ have been obtained as 9.6 dB/km and 9.5 dB/km respectively. This assumes the uniform attenuation rate in the catchment area.

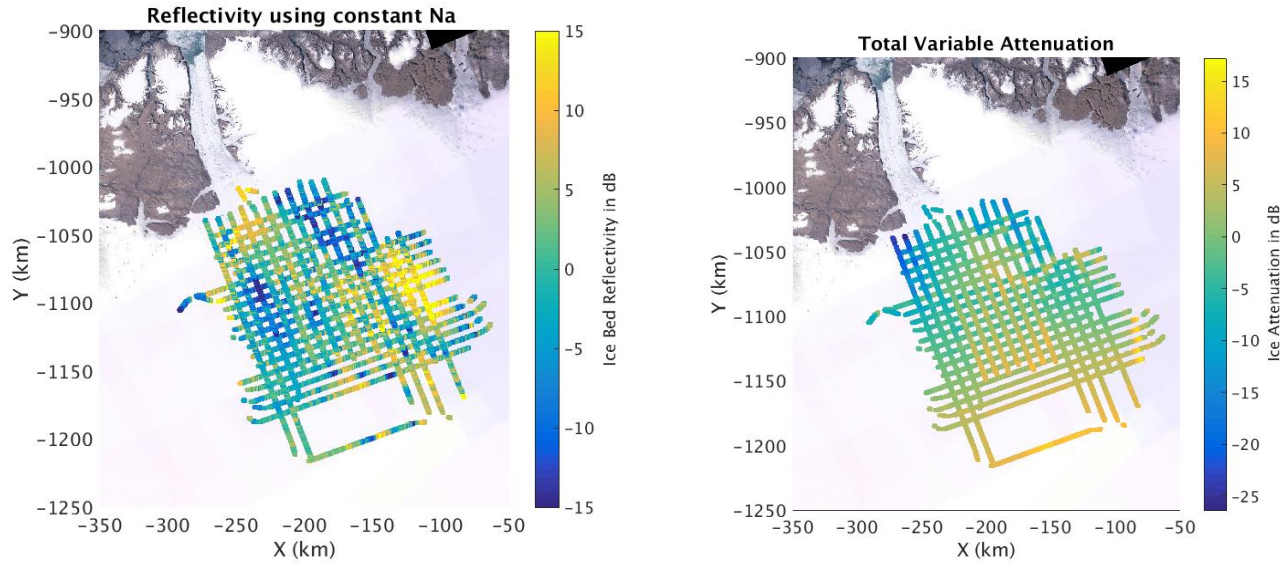


Figure 4.10 Ice Bed Reflectivity using uniform attenuation rate (right), Total ice attenuation (left)

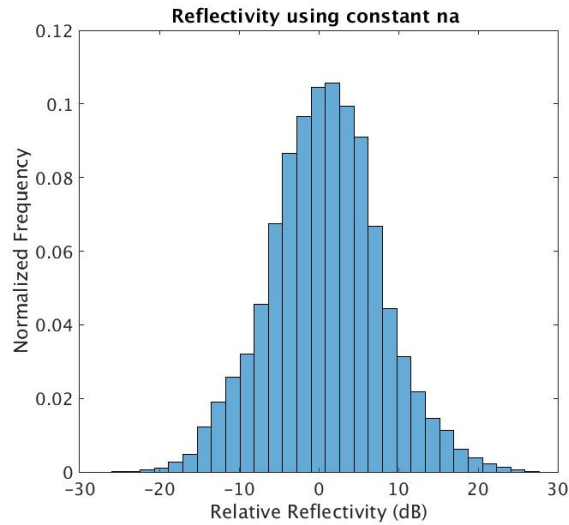


Figure 4.11 Range of Relative Reflectivity

Fig. 4.10 (left) shows the ice bed reflectivity following uniform attenuation method. Fig. 4.11 shows the range of reflectivity values. The uniform attenuation rate does not capture the attenuation rates near the ice margins where the attenuation rate is higher (Chu et. al, 2016) as well as the total ice attenuation at the cross over between seasons have larger mismatch shown in Fig. 4.10 (right) hence the variable attenuation rate calculation method is required to address the issue.

As described in Chapter 2.3.3, first the geometrically corrected bed power and ice thickness is filtered using a long filter of 30 km to capture the overall trend of the catchment area and fit to Eq. (2.29) to calculate the mean attenuation rate $\overline{N_a}$ of 9.3142 dB/km and 9.3228 dB/km for 2011 and 2012 seasons. This is used as input for the variable attenuation method where the along track derivative of attenuation rate $\frac{\partial N_a}{\partial x}$ was calculated by fitting the geometrically corrected ice bed echo filtered for 1.5 km in each line to corresponding filtered depth at 1.5km as given in Eq. (2.31). The modified attenuation rate is then calculated using mean attenuation rate $\overline{N_a}$ and along track derivative of mean attenuation rate $\frac{\partial N_a}{\partial x}$ given by Eq. (2.32).

Fig. 4.12 (c) shows the apparent attenuation $-P_r^c$ which is the value required to make ice bed reflectivity zero. This assumption helps in the initial estimate of ice attenuation rate which corresponds to the ice thickness in Fig. 4.12 (d). Here there is sufficient variation in depth and relative power as shown in Fig. 4.12 (b) and thus the modelled attenuation is able to compensate for the increasing attenuation rate towards the margin. Fig 4.12 (e) shows the modelled attenuation rate (red) and apparent attenuation (blue). The resulting reflectivity is the deviation of ice bed power from the modelled attenuation shown in Fig 4.12 (f).

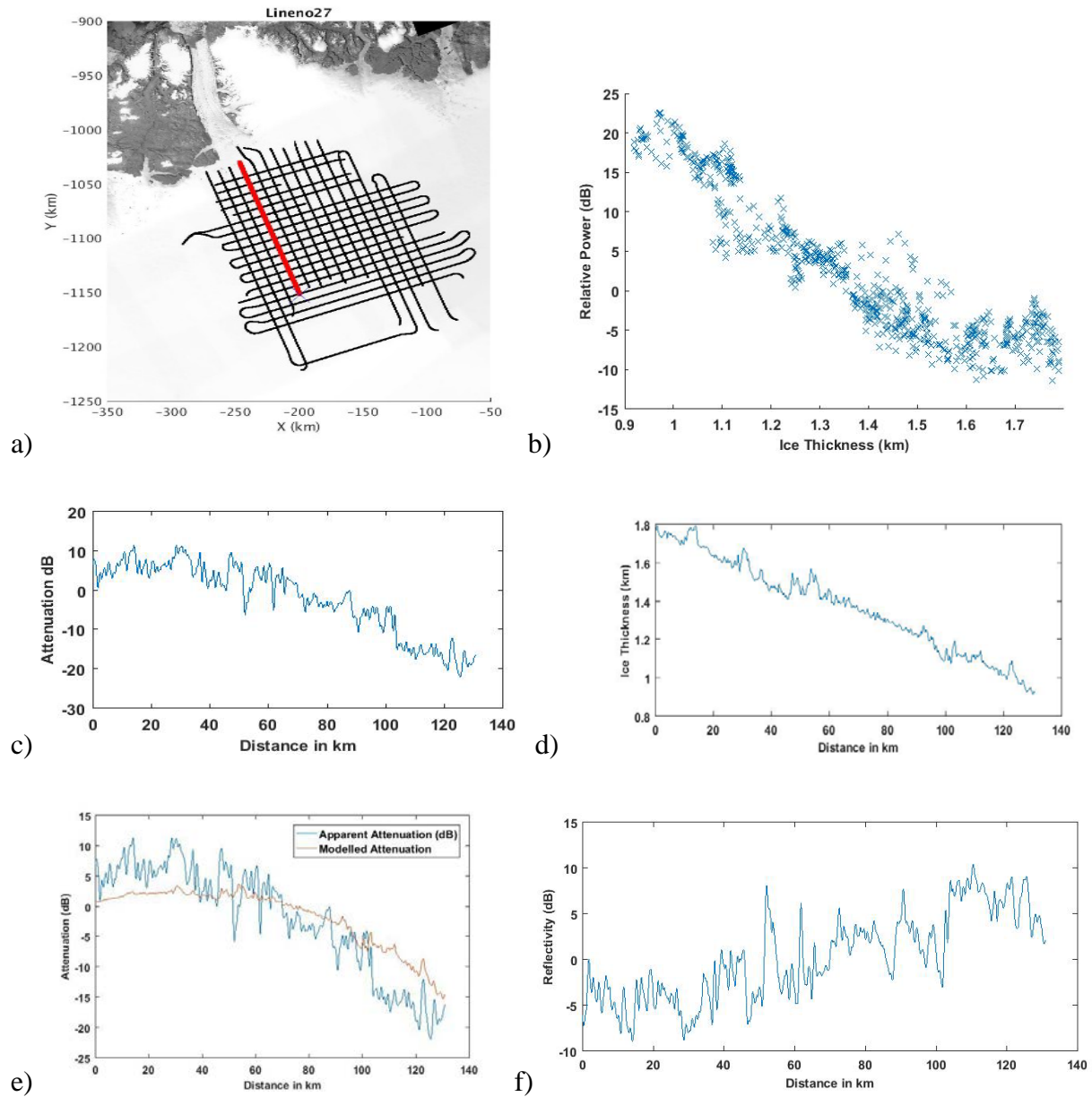


Figure 4.12 Radar Line extending from ice interior to ice margin (a), Relative Ice Bed Power versus Depth profile (b), Apparent Attenuation (c), Ice Thickness (d), Modelled Attenuation (Red) and Apparent Attenuation (Blue) using variable attenuation method (e)

Fitting geometrically corrected ice bed echoes with depth to calculate the local rate of change of attenuation requires sufficient variation in ice thickness and attenuation in order to estimate the attenuation rate which puts the constraints on segment used for fitting (Schroeder et al., 2016). These criteria are often met when the survey lines extend from central ice towards ice

margin where there are both variations in depth and attenuation rate as shown in Fig 4.12 (a). However, the sufficient fitting length criteria is not met when thickness variation is small.

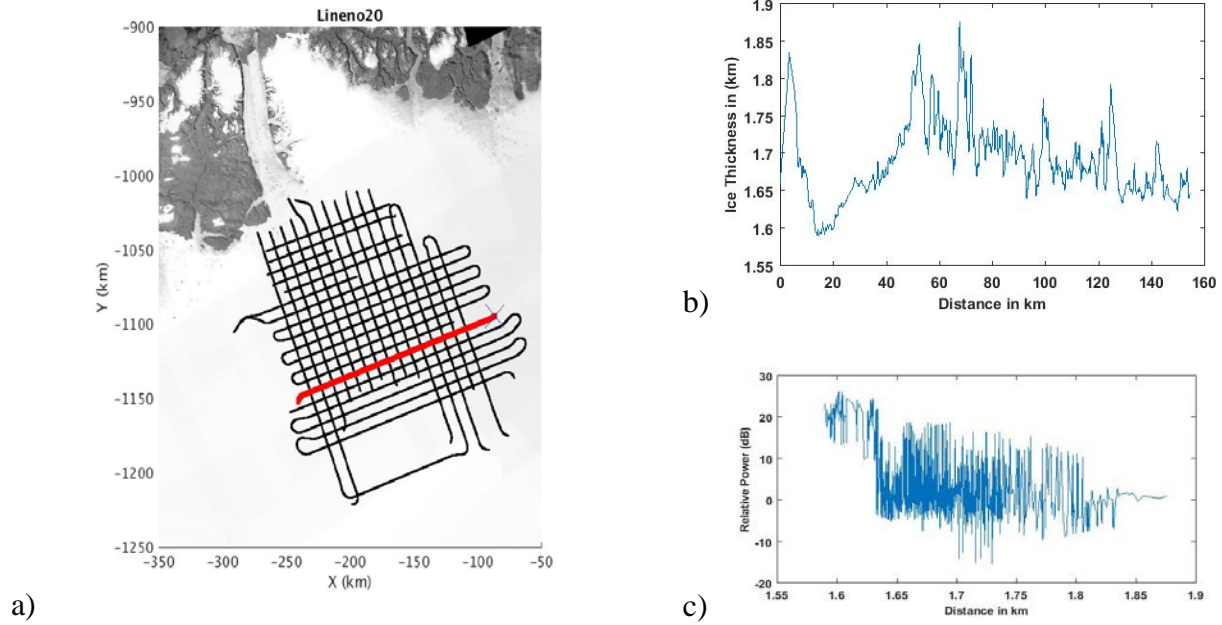


Figure 4.13 Radar Survey Line (a), Ice Thickness Profile along the Survey Line (b), Relative Power along depth profile (c)

Fig. 4.12 shows the application of variable attenuation method which uses the variation in depth and relative power to model the attenuation. Fig 4.12 (a) shows the radar survey line extending from ice interior towards the ice margin. Fig 4.12 (b) shows the relative ice bed power and its variation with the depth profile. This variation in depth is important to calculate $\frac{\partial N_a}{\partial x}$ by using Eq. (2.31). Fig. 4.13 (a) shows the radar survey line in the catchment area with lesser ice thickness variation in Fig 4.13 (b). Fig 4.13 (c) shows relative ice bed power along the depth profile. Here the variation depth is very less and hence the fitting to calculate $\frac{\partial N_a}{\partial x}$ is ill poised. As described in Schroeder et al., 2016, the fitting segment length should be small for the areas with large ice thickness and should be longer with good topographic relief for areas with smaller ice

thickness to achieve comparable radiometric resolution. So the modified attenuation calculated from this method cannot be applied to every radar lines as sufficient fitting criteria is not met.

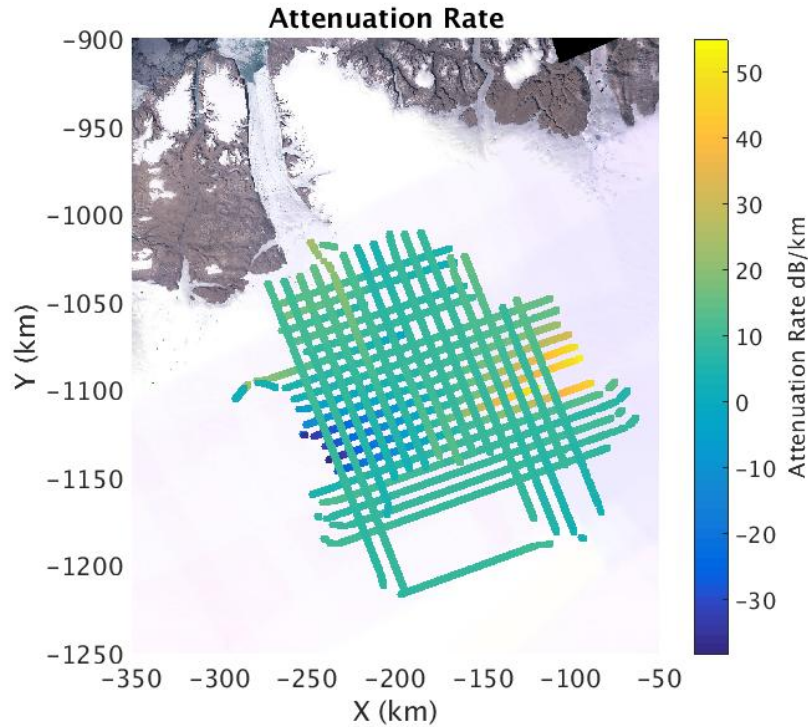


Figure 4.14 Attenuation Rate calculated from variable attenuation method

Fig. 4.14 shows the attenuation rate estimation to be comparable to ice attenuation estimation from Chu et.al, 2018 for the longitudinal lines however, is not physically realizable for crosslines as negative attenuation rate is not possible. In order to solve this issue, the attenuation rates for the crosslines has thus been calculated by interpolating using the attenuation rate of the longitudinal lines at the crossovers.

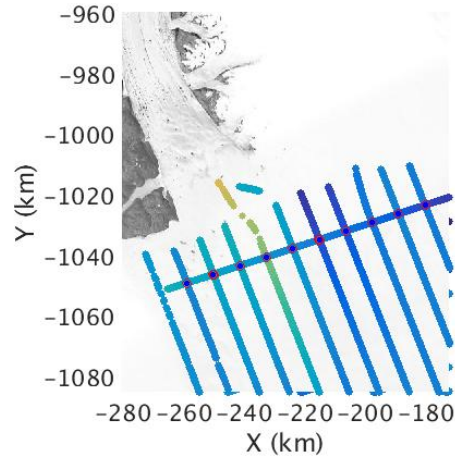


Figure 4.15 Attenuation Rates at Cross over Locations

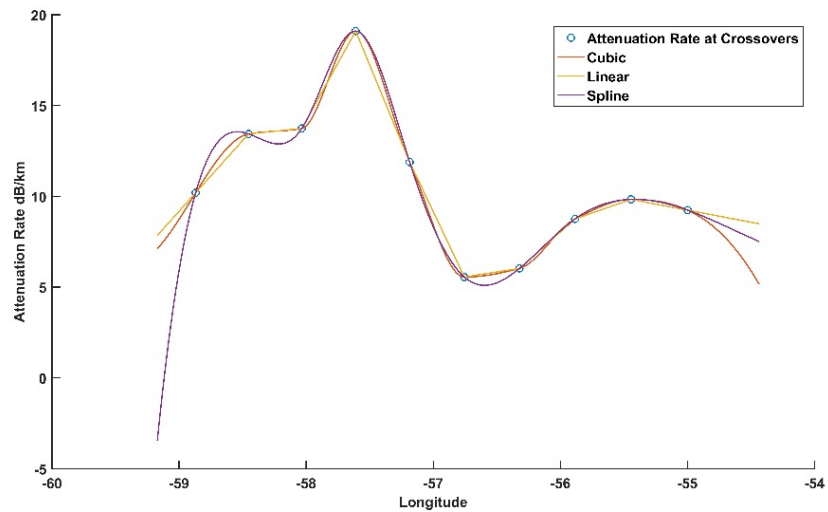


Figure 4.16 Interpolation of Ice Attenuation rate from Crossover using different interpolation techniques

Among the interpolation methods cubic interpolation seemed to be more reasonable choice of interpolation to capture the gradual attenuation rate change. Fig. 4.15 shows the cross over points and Fig. 4.16 shows the attenuation rate from longitudinal lines at the crossover where

different interpolation methods are applied. The attenuation rate for the catchment area thus obtained is shown in Fig. 4.17.

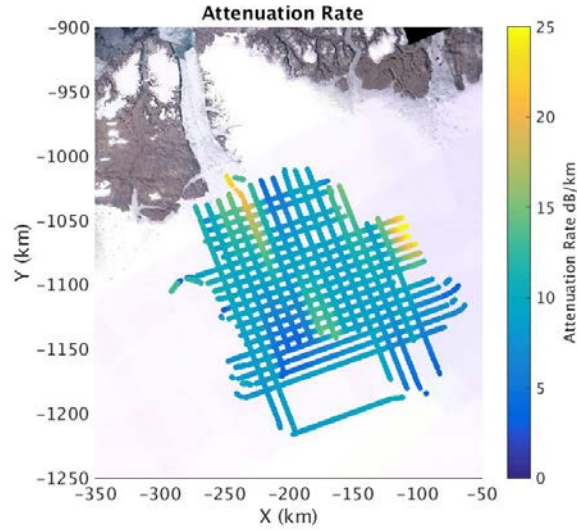


Figure 4.17 Attenuation Rate using interpolation method

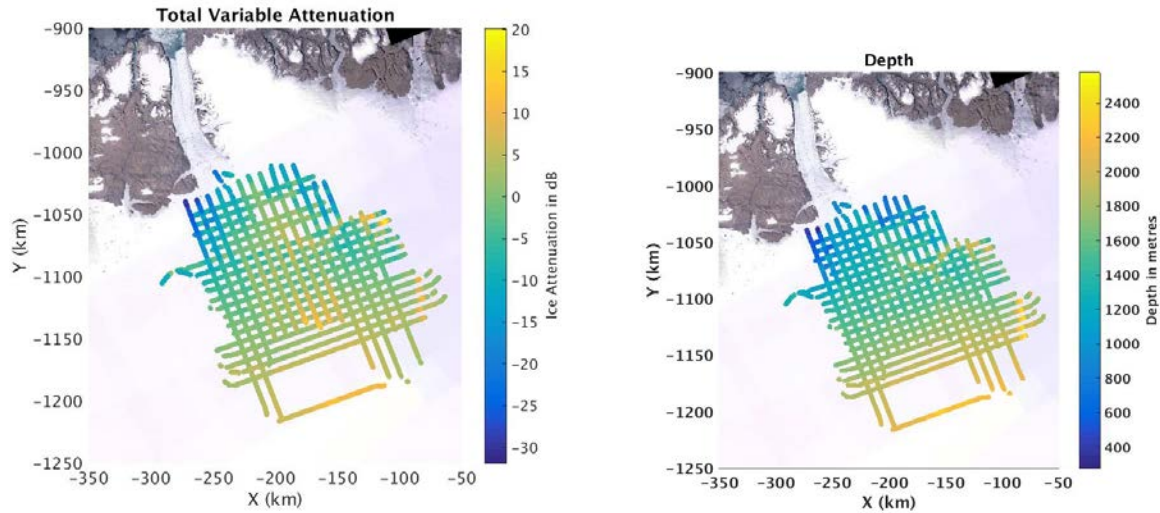


Figure 4.18 Total Ice Attenuation (left), Depth (right)

This method of attenuation rate calculation is effective in estimating the basal reflectivity however is less suited if there are nonlinear attenuation rate changes. However, in our case this

attenuation rate calculation method is sufficient in constraining and revealing the patterns of the ice bed reflectivity.

The total variable ice attenuation was thus estimated by using variable attenuation model as shown in Fig. 4.18 (left). Since there are two seasons with different attenuation rates, mismatch can be seen towards the center of the glacier but within a season a good degree of match at cross over can be found. The total ice attenuation is more comparable than using the uniform attenuation rate. Fig 4.18 shows the total attenuation and its corresponding depth. Even at the shallower regions towards the ice margin, total ice attenuation is large due to higher attenuation rate.

4.2.3 Ice Bed Reflectivity of Peterman Glacier

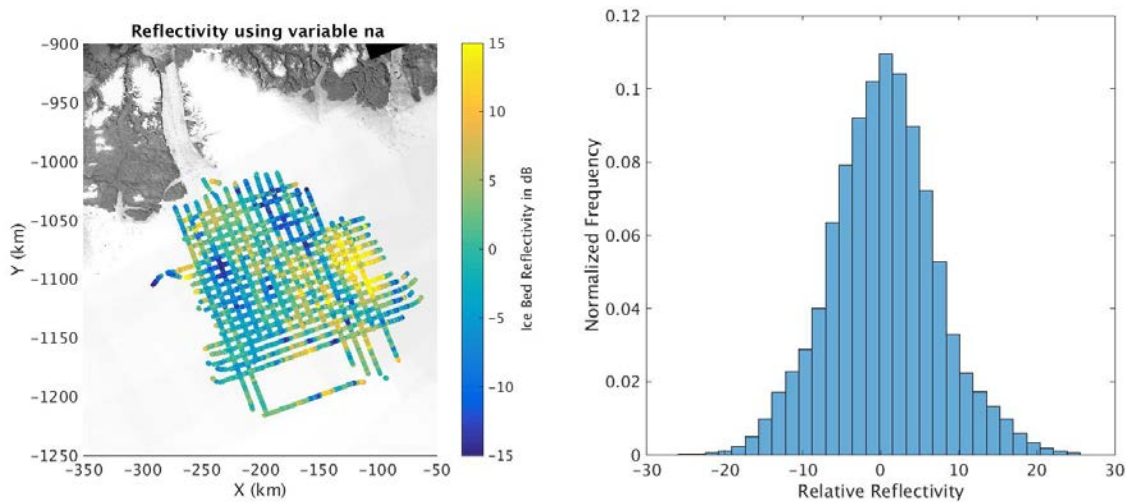


Figure 4.19 Relative Ice Bed Reflectivity (left), Range of Relative Reflectivity Values (right)

The estimated ice bed reflectivity after rough surface corrections and ice attenuation loss corrections is shown in Fig. 4.19 (left). Fig. 4.19 (right) shows the range of reflectivity values. Compared to reflectivity values calculated using uniform attenuation rate in Fig. 4.10 (left), the effects due to variable attenuation rate can be seen towards the ice margins where the reflectivity

value is lowered following the variable attenuation rate as shown in Fig 4.19(left). There is also decrease in the number of reflectivity values greater than 10 dB.

Since the bed roughness is small in the catchment region, the resulting bed reflectivity map represents the effect due to bed dielectric constant. Higher reflectivity is usually interpreted as wet beds and lower reflectivity as frozen beds (Macgregor et al., 2016; Schroeder et al., 2016; Chu et al., 2018). Here the areas with higher reflectivity greater than 10 dB is interpreted as wet beds or presence of basal melting (Chu et al., 2017).

4.2.4 Discussion and validation of ice bed reflectivity result

Next, we will validate the ice bed reflectivity results using cross over analysis, geophysics, ice bed topography, hydraulic potential, ice surface speed, abruptive index and also compare them with previous studies.

1. Crossover Analysis

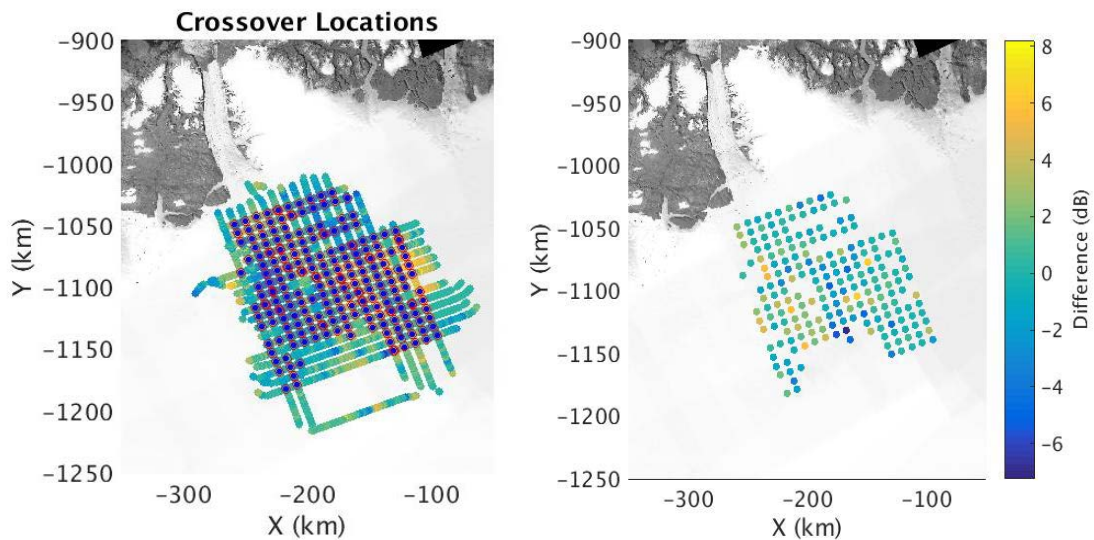


Figure 4.20 Crossover Locations (left), Ice Bed Reflectivity Difference (Right)

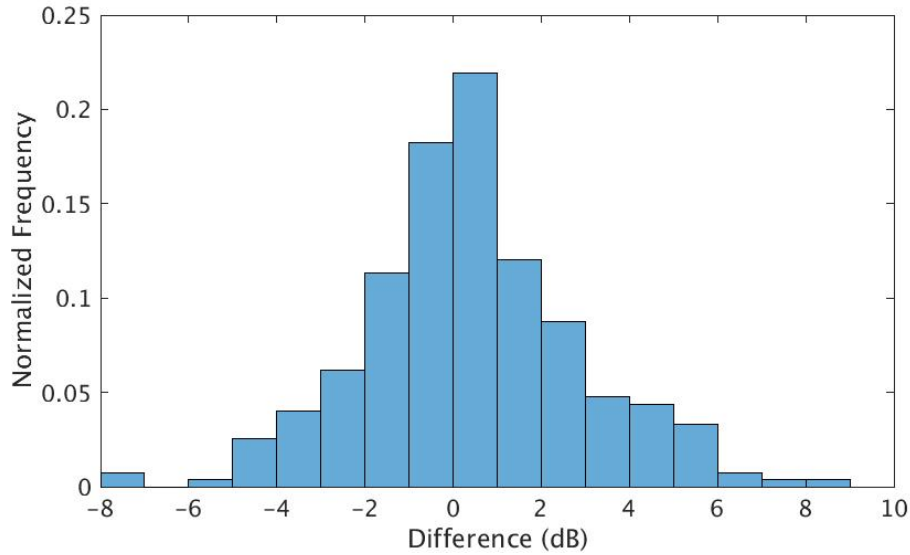


Figure 4.21 Reflectivity difference at cross over locations

Crossover analysis at locations shown in Fig. 4.20 (left) was done for longitudinal and lateral lines with crossover search radius of 100 meters. As shown in Fig. 4.20 (right) and Fig. 4.21, crossover analysis of ice bed reflectivity shows most areas match with each other with 93.6% of the crossovers within 5dB difference and 81.3% within 3 dB difference. The ice bed reflectivity calculation assumes isotropic bed, and the crossover mismatch may include anisotropic effects of the bed which includes bed geometry and slope effects.

The variable attenuation method assumes constant reflectivity from all interfaces in calculating the ice attenuation, and hence there is a tradeoff between ice bed reflectivity and ice attenuation calculations. Most crossover errors exist in the crossover between the seasons, and some contribution may also come from the change in the ice conditions over the period of time.

2. Geophysics

The areas identified with basal melting have distinct features as compared to frozen beds. Fig. 4.22 shows the location of area with higher reflectivity (left) and its corresponding reflectivity (right). Fig. 4.22 also shows the echogram with relatively high local intensity with high dielectric contrast and the areas to be relatively flat so that basal melt can be present. Similarly, the angle of internal layers dipping is greater than the bed topography shown in the rectangular box which all point to the presence of basal melt.

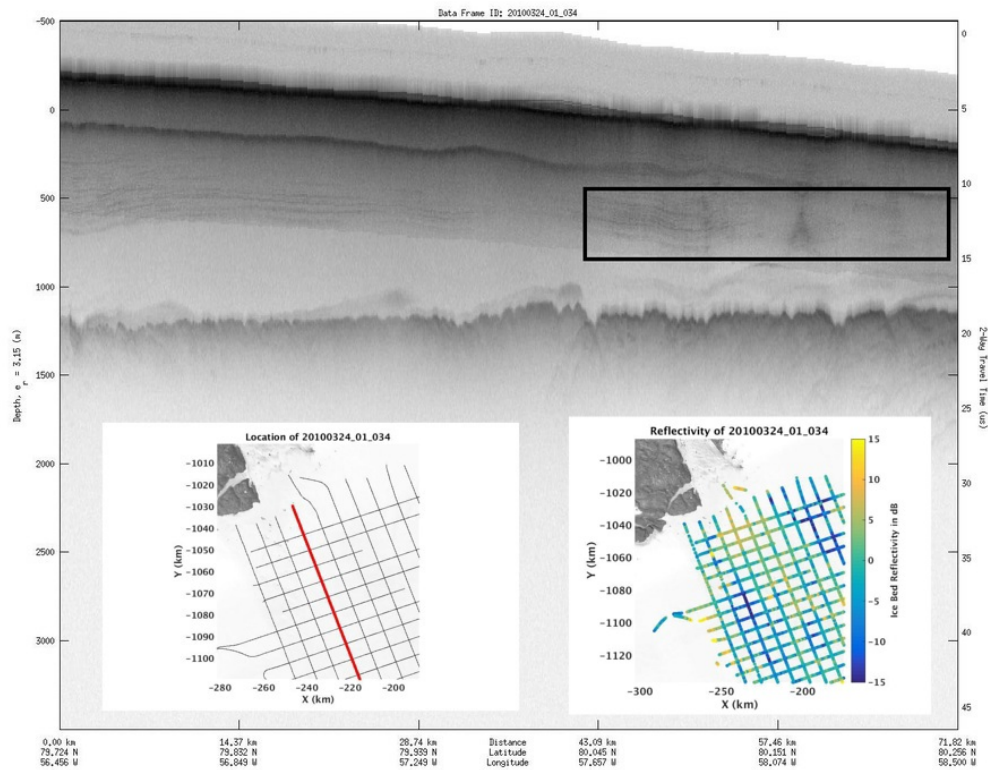


Figure 4.22 Echograms showing areas of basal melt

For this frame we can plot the ice bed reflectivity along with its abruptive index and coherence index as shown in Figure 4.23. It can be observed that the areas with high reflectivity

correlates with high abruptive index and coherence index. Since areas with basal melt usually have high abruptive index and high reflectivity we can infer that there is the presence of basal melt at this location.

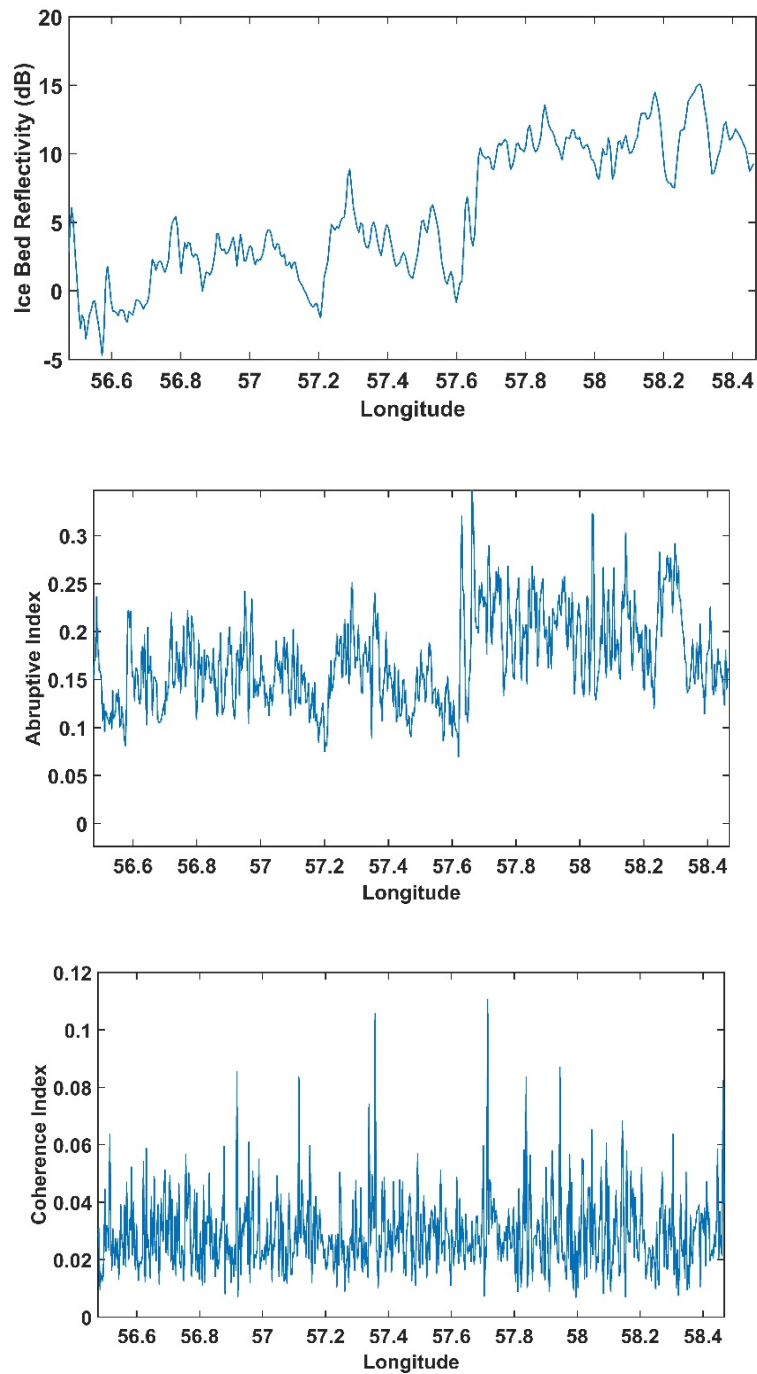


Figure 4.23 Ice Bed Reflectivity, Abruptive Index and Coherence Index for 20100324_01_034

3. Basal Melting and Bed Topography

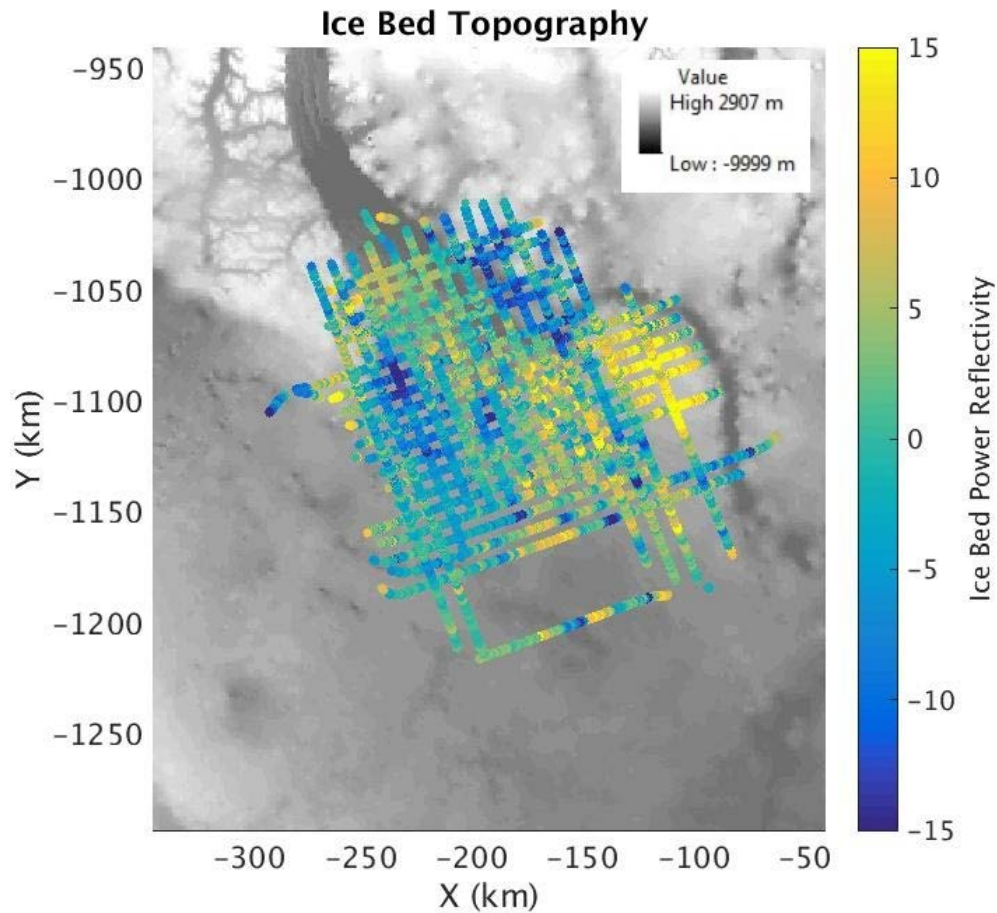


Figure 4.24 Ice Bed Reflectivity from this study plotted over Ice Bed Elevation Map

The ice bed reflectivity is overlapped on the bed elevation map (Bamber, 2001) in Fig. 4.24. We observe the reflectivity values are higher towards the trunk of the glacier with low bed elevation. Bed topography of Petermann glacier also reveals the paleofluvial canyon across eastern margin but it has lower reflectivity thus routing of subglacial water through this channel has not been observed. Instead the higher bed elevation zone at eastern margin has higher reflectivity. The continuous evolution of Petermann glacier may likely cause basal water to route through the paleofluvial canyon towards the ice margin in near future.

4. Basal Water and Ice Surface Speed

It has been established that the ice surface speed correlates with basal water on areas with less topographic constraints (Jordan et al., 2018). As shown in Fig. 4.25, the ice bed reflectivity has been plotted against ice surface velocity determined using interferometric SAR (Joughin et al., 2016) and the correlation is evident in which the fast moving ice ($>150\text{m/year}$) near the trunk correlates with higher reflectivity. Similarly, the western shear margin where the reflectivity is low corresponds with slower ice surface speed ($<40\text{ km/year}$).

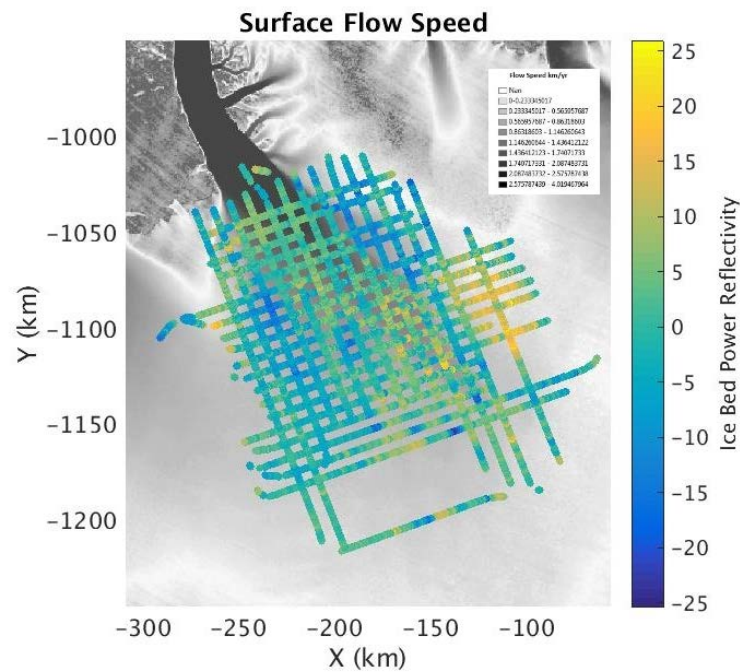


Figure 4.25 Ice Bed Reflectivity from this study plotted over Ice Surface Speed Map (Joughin et al., 2010)

5. Basal Water and Abruptive Index

Oswald and Gogineni, 2008 explained that the abruptness of the received echo is also indicative of the basal water as there is sharp transition in the dielectric giving rise to specular

echoes provided that the echo intensity is also high. So areas with both higher abruptive index and higher bed echo power are often indicative of basal melt. It can be observed from Fig. 4.26 that the comparison of abruptness and ice bed reflectivity gives areas where both correlate with each other. In some areas the abruptness is low but the reflectivity is high which may be due to the roughness of the surfaces otherwise they are in good agreement with each other.

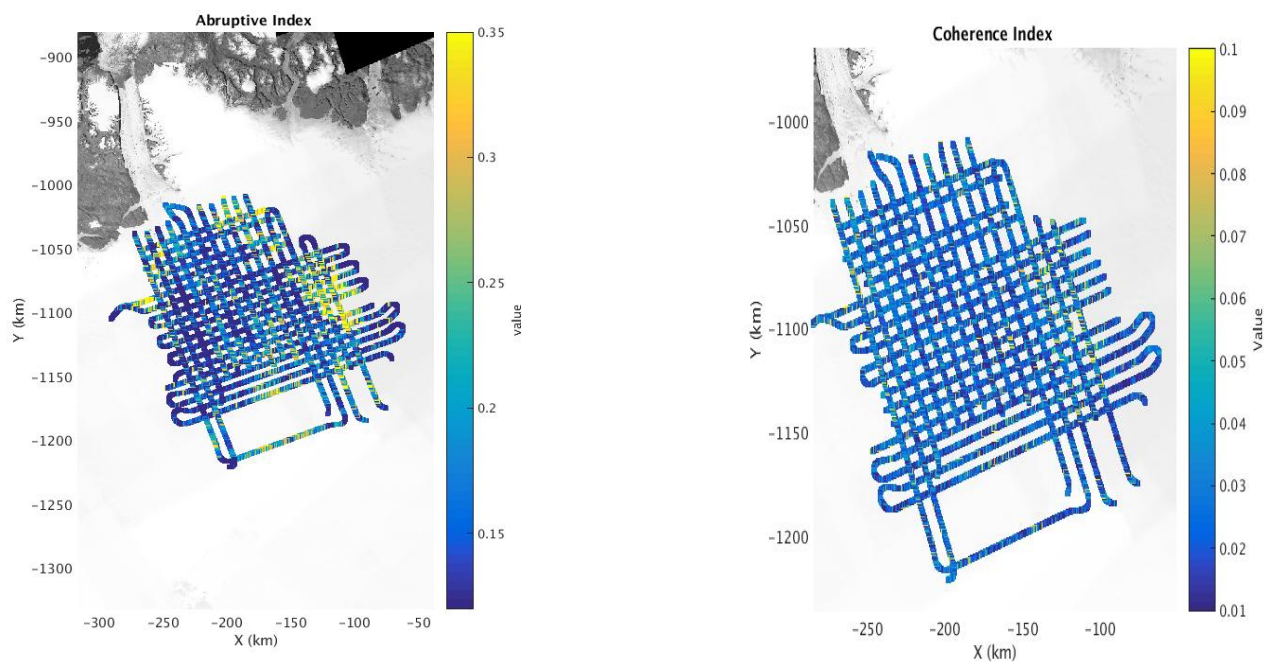


Figure 4.26 Abruptive Index Map (left) and Coherence Index Map(right) for Petermann Glacier

Coherence index calculated from the data does not reveal much about the basal condition but some degree of correlation can be observed at places with higher reflectivity.

6. Comparison with Previous studies

The reflectivity pattern matches with the previous models and data inversion techniques (Macgregor et al., 2016; Chu et al., 2016) that the areas near the trunk of the glacier has thawed

bed and frozen beds in the shear margins. Fig. 4.27 displays areas of higher reflectivity (>10 dB) from this study and from W. Chu et al., 2016 which uses the thermomechanical modeling of ice sheet to derive the basal conditions. It can be observed that most of the areas of higher reflectivity corresponds to the basal melts as predicted by Chu.

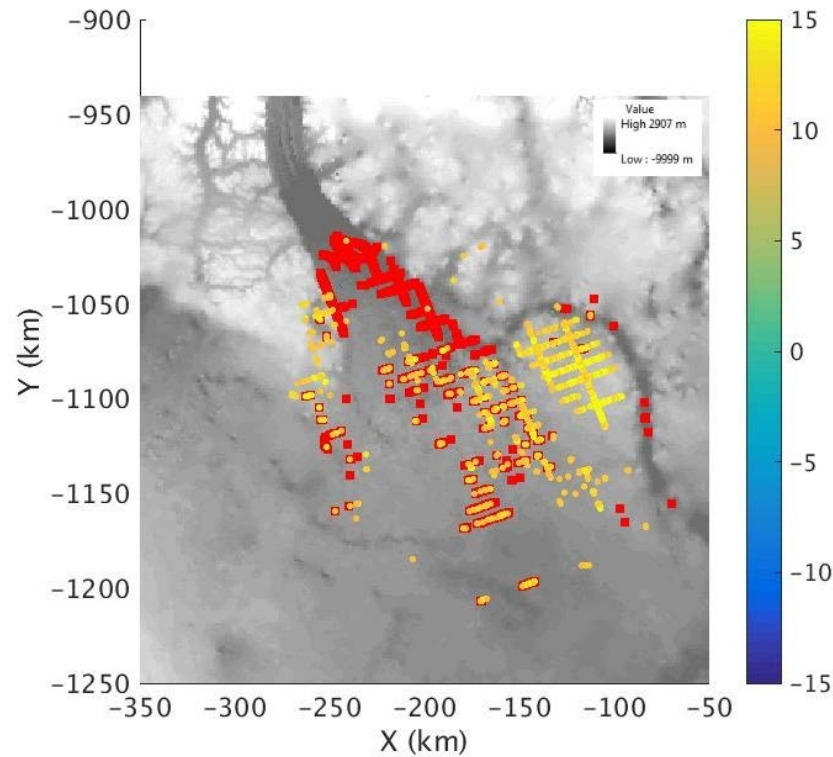


Figure 4.27 Areas of basal melting from this study (yellow) compared with previously identified areas of basal melting (red, Chu et al., 2016)

However, there are certain areas where results do not match well. One of the areas towards the eastern shear margins the reflectivity has been observed as high but the location has frozen bed as predicted by Chu et al., 2017. The major mismatch is towards the trunk of the glaciers where this study presents moderate reflectivity values while these locations were reported to have large reflectivity values. The SAR processed data for 2010 used by Chu et. al is square of the bed power

instead of the bed power (an ignorance that will be corrected by CReSIS), resulting in the reported 43.7dB offset between bed power from 2010 and 2011 seasons at crossovers. Even this offset was removed by leveling, the use of square of the ice bed power would lead to larger reflectivity towards the trunk for 2010 data and falsely interpreted as basal water in Chu's study. Our results however show moderate reflectivity at the trunk. On the other hand, the ice bed reflectivity for 2011 season matches well between the two methods as shown in Fig. 4.27.

The ice bed reflectivity map of Petermann glacier thus reveals areas with frozen and wet beds with higher correlation with its surface flow speed. Due to the lack of a topographic feature to prevent the ice slow, Petermann glacier is vulnerable to the ice flow speed and may continue losing ice mass in coming years.

4.3 Basal Conditions of Jakobshavn Glacier

Jakobshavn glacier has a very high flow rate and is losing a lot of ice. It has several characteristics, such as the discharge of large amounts of land-based ice to floating ice, channels with over-deepened beds and negative bed slopes, grounding zones in contact with the ocean, and rough, crevassed surfaces (Gogineni et al., 2014). The measurement of this glacier's ice thickness has been a major challenge due to its extremely rough surface and the presence of temperate ice at its bed (Gogineni et al., 2014). The bed topography of Jakobshavn also shows channels along the glacier that facilitates the ice flow into the margin. Hence it is important that this unstable glacier needs to be studied further to understand its ice dynamics.

4.3.1 Roughness Estimate for Jakobshavn Glacier

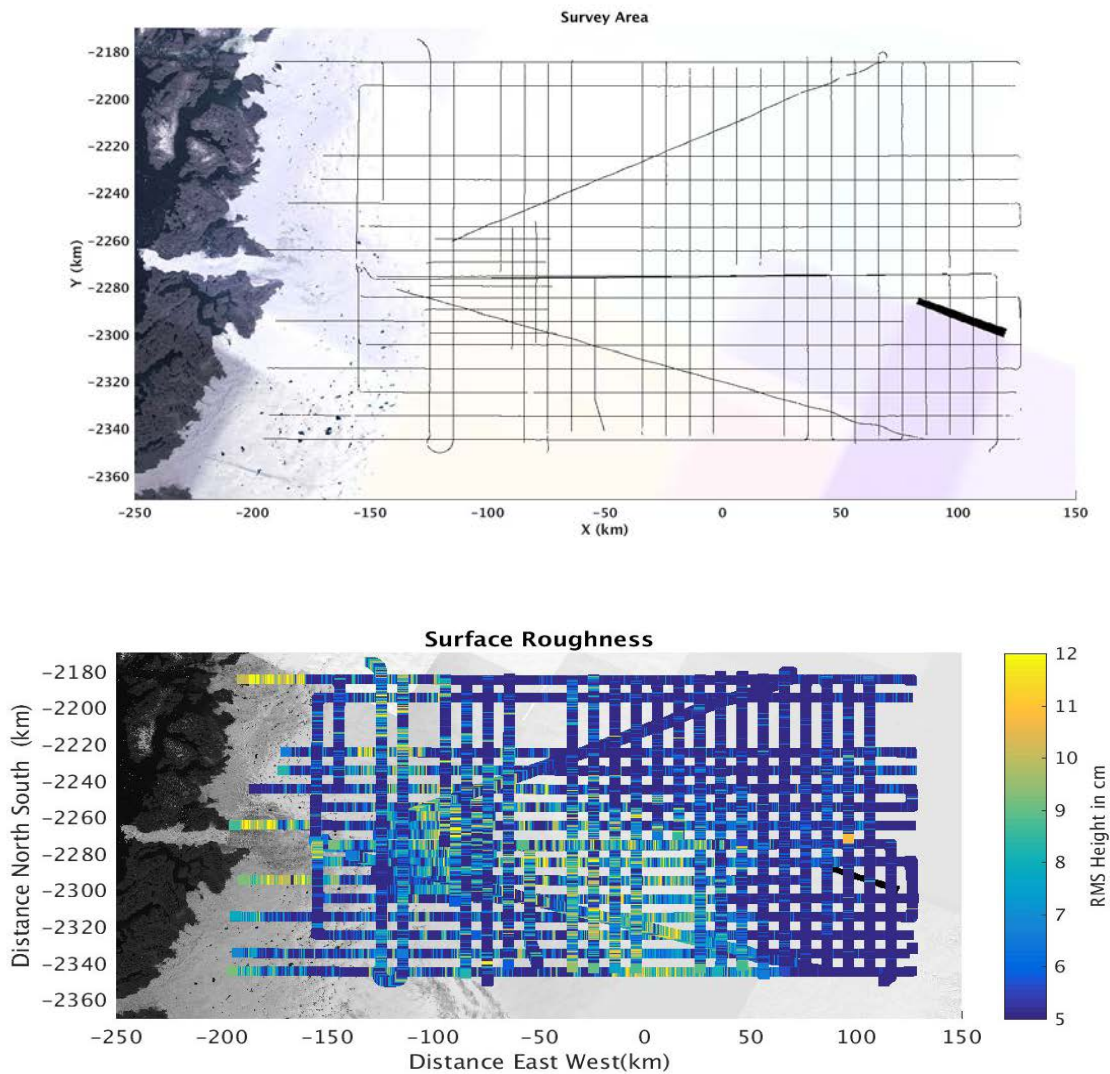


Figure 4.28 Survey Area with Radar Lines (top), Surface Roughness derived from MCoRDS (bottom)

Fig. 4.28 (top) displays the flight lines over the study area of Jakobshavn glacier. Fig. 4.28 (bottom) presents the roughness estimates of Jakobshavn glacier by applying RSR to Jakobshavn data. It is evident that much of the surface towards the center of the ice sheet is smooth. In contrast, as we move towards the coast, the surface becomes rougher. It is evident that Jakobshavn glacier's

ice margin is majorly crevassed near the calving fronts with more complex patterns which is very well identified from the surface roughness map as shown in Figure 4.28. Within the glacier front some crevasse free locations also exist where roughness is pretty low.

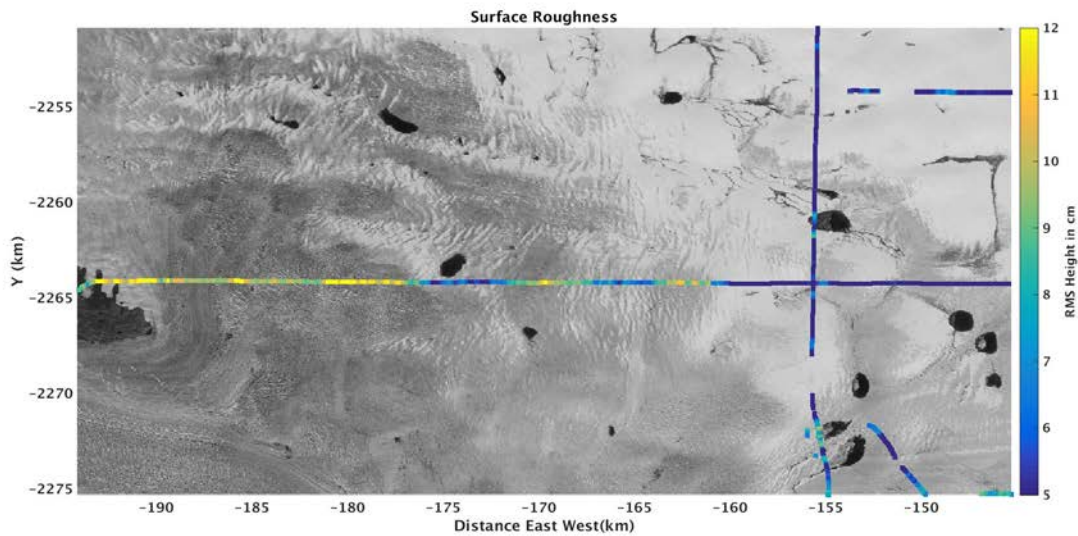


Figure 4.29 Surface Roughness overlaying Landsat Image at Jakobshavn

Fig. 4.29 shows that surface roughness is higher towards the margin and lower towards the ice interior. Crossover analysis of surface roughness yields agreement at most crossover locations except at few locations near the ice front where the surface complexity is very high.

For bed roughness of Jakobshavn glacier, the unfocused SAR is not able to resolve the bed echoes properly because of the surface clutter and large attenuation through the temperate ice. A 5-dB SNR (Signal-to-Noise Ratio) criterion removes weaker bed echoes from the data especially in the deeper ice sheets where SAR processing is required for the additional increase in SNR. The bed roughness is then calculated for the areas with sufficient ice bed echoes. The bed is rougher towards the ice margin as expected shown in Fig. 4.30.

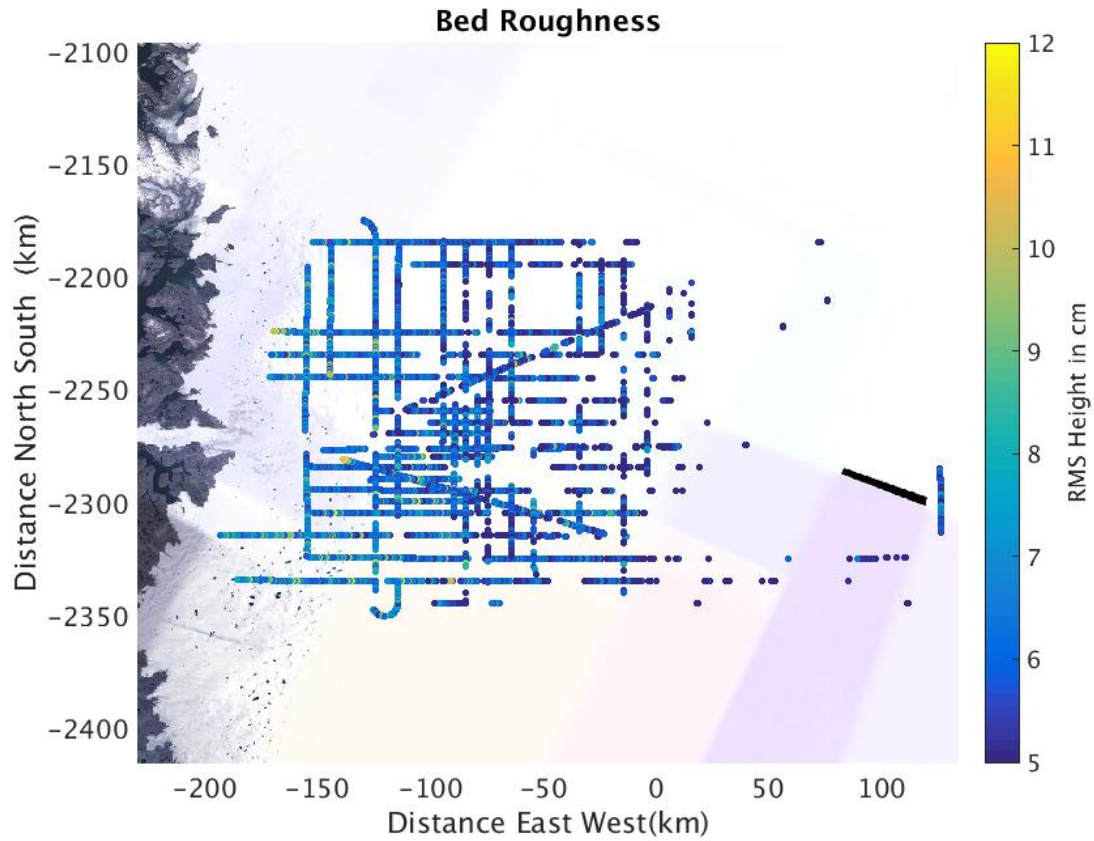


Figure 4.30 Ice Bed Roughness

4.3.2 Ice Attenuation Estimation of Jakobshavn Glacier

Fast flowing glaciers and ice-sheet margins have very rough surfaces because of extensive crevassing (Gogineni et al., 2014). It is difficult for proper airborne radar sounding in these regions because of the rough surfaces and large ice attenuation through the temperate ice. However, SAR processing to reduce the along-track clutter and arrays to reduce cross-track surface clutter have been used to process the Jakobshavn data to fully resolve the ice bed echoes with along-track resolution of 30 meters.

Here the SAR processed data have been used for this glacier to analyze the ice attenuation estimation and ice bed reflectivity. Radar survey lines extending from North to South and East to West are used as grids. The ice bed power has been corrected for surface roughness losses, and geometric losses to obtain corrected ice bed power. A regression fit of this corrected ice bed power against depth as shown in Fig. 4.31 gives constant attenuation rate of 10.3 dB/km for the glacier.

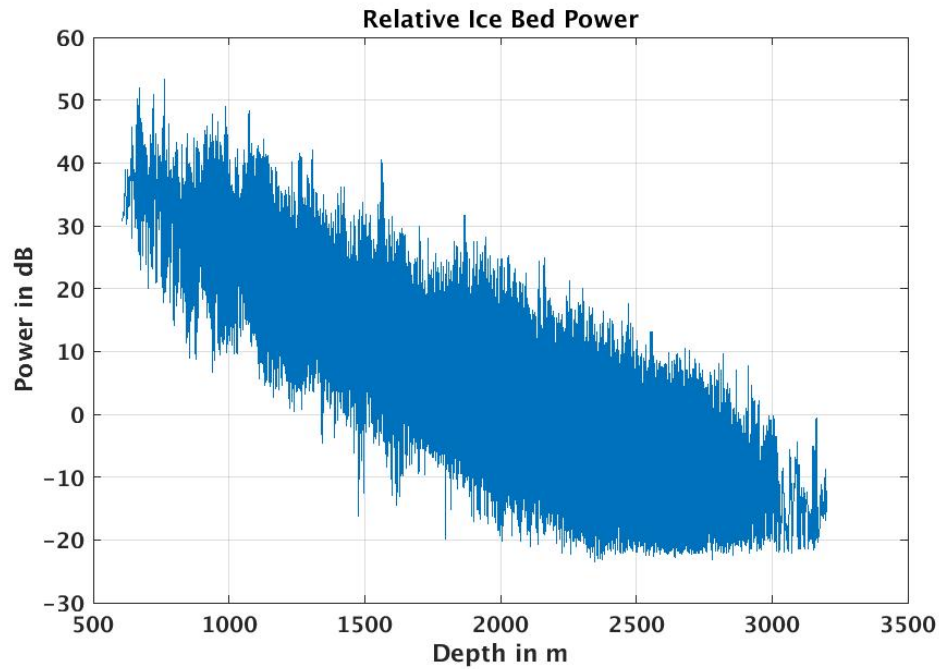


Figure 4.31 Geometrically corrected ice bed power plotted with corresponding ice depth

As discussed in Chapter 3, the modified attenuation rate is then calculated for each radar line by deriving rate of change of attenuation by local scatter based fitting to estimate total ice loss. However, this method only works when there is a linearly varying attenuation rate across each radar line.

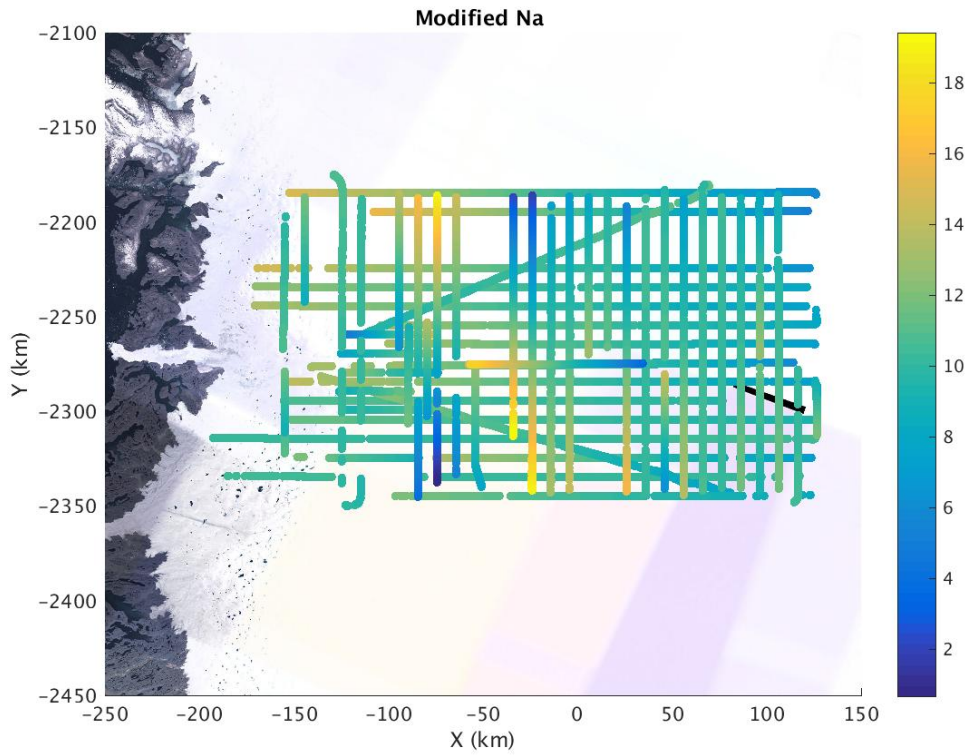


Figure 4.32 Attenuation Rate at Jakobshavn using variable attenuation rate method

Figure 4.32 shows the attenuation rate calculated for Jakobshavn glacier using variable attenuation method. The attenuation rate is increasing from the ice interior towards the coast as expected whereas for longitudinal lines the trend is random. The limitation of variable attenuation method is that it works only for linearly varying attenuation rate and fails whenever there is non-linearly varying attenuation rate. The fitting requires sufficient variation in ice thickness and attenuation within a radar line to accurately estimate the attenuation rate (Jacobel et al., 2010) which puts a constraint on the size of the segment used for fitting (Schroeder et al., 2016). This condition is not met by longitudinal lines as depth across these lines are relatively constant.

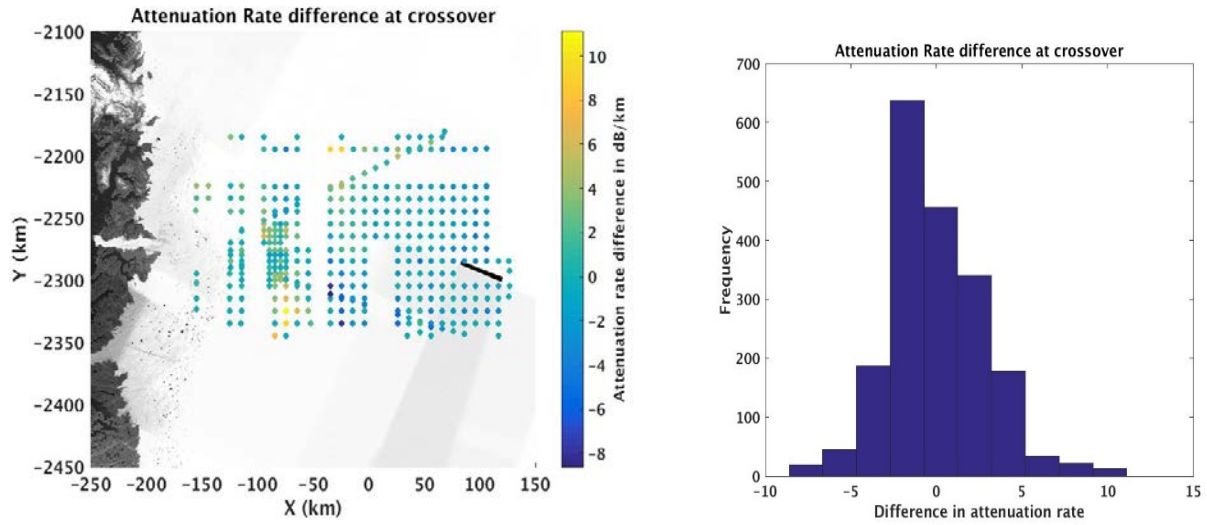


Figure 4.33 Attenuation Rate difference at crossover locations (left), Histogram of attenuation rate difference in dB/km at crossover locations (right)

Fig. 4.33 (left) and Fig. 4.33 (right) shows the mismatch of attenuation rates at crossover locations following the variable attenuation rate method. The mismatch between the attenuation rates shown by Fig. 4.33 at several locations suggest that variable attenuation models is not able to compensate for the non-uniform attenuation rates at Jakobshavn glacier. Since it can only work for linearly variable attenuation rate which is true for lines extending from deeper ice sheets towards the shallower ice margin, the variable attenuation rate method has been applied to these lines. The ice attenuation rates for the longitudinal lines are then interpolated using the crossovers. Fig. 4.34 and Fig 4.35 presents the englacial attenuation rate and total englacial attenuation obtained for the Jakobshavn glacier.

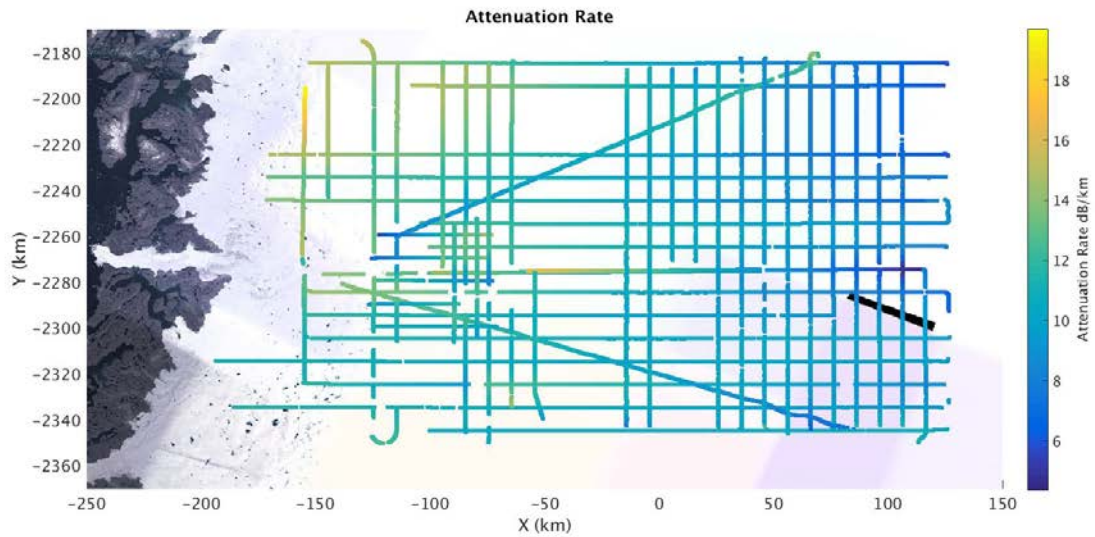


Figure 4.34 Attenuation Rate (dB/km) across Jakobshavn Glacier applying linearly variable attenuation rate method

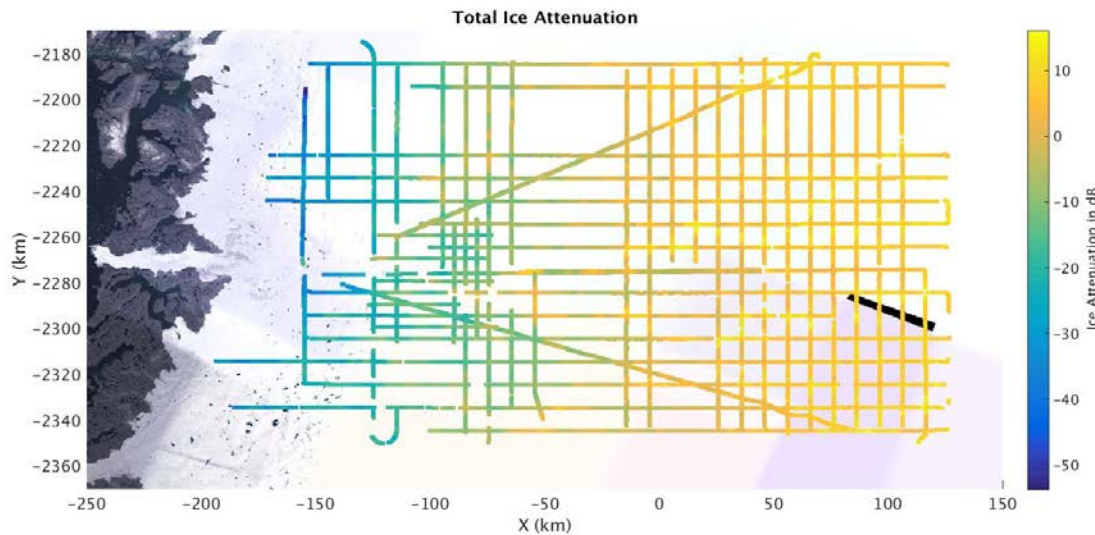


Figure 4.35 Total ice attenuation at Jakobshavn glacier

Consistent with previous studies from MacGregor, 2014 the ice attenuation rate is smaller towards the central ice and larger towards the ice calving fronts with temperate ice causing more loss towards the ice margins (Macgregor, 2014).

4.3.3 Ice Bed Reflectivity of Jakobshavn Glacier

Fig. 4.36 presents the estimated ice bed reflectivity map for Jakobshavn glacier, which shows most of the areas in the catchment area of Jakobshavn glacier is likely thawed as represented by the areas with higher reflectivity. This may be one of the reasons that ice flow in Jakobshavn glacier is very high with basal lubrication helping in sliding of ice sheet more easily.

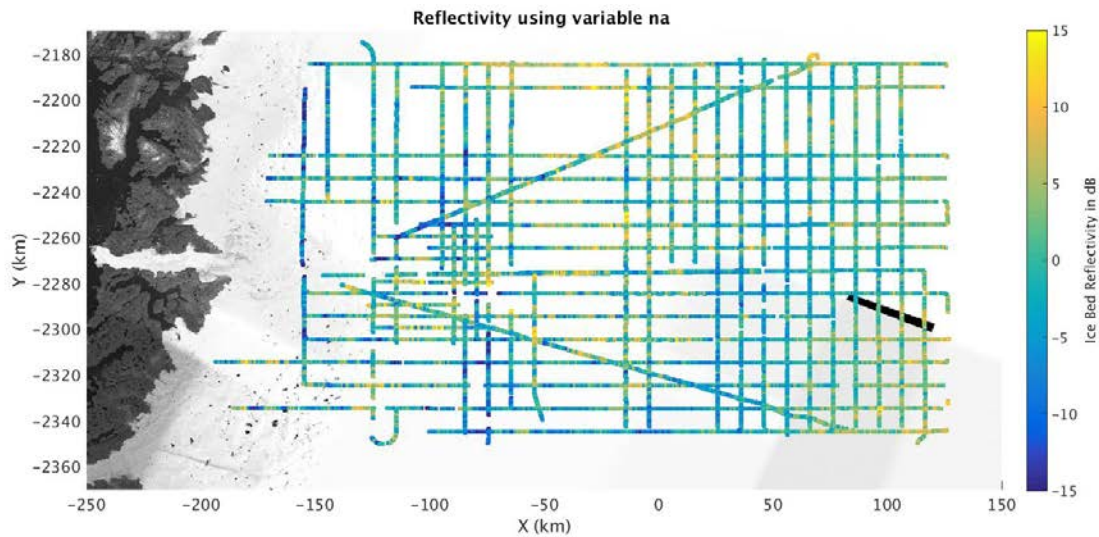


Figure 4.36 Ice Bed Reflectivity of Jakobshavn Glacier

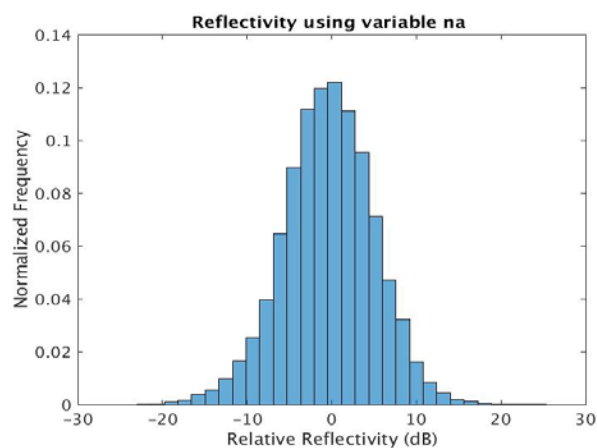


Figure 4.37 Histogram showing the range of relative ice bed reflectivity values

Figure 4.37 shows the range of relative ice bed reflectivity values. The relative reflectivity values greater than 10 dB are represented as areas with basal melting (Chu et al., 2016) and shown in Fig. 4.36.

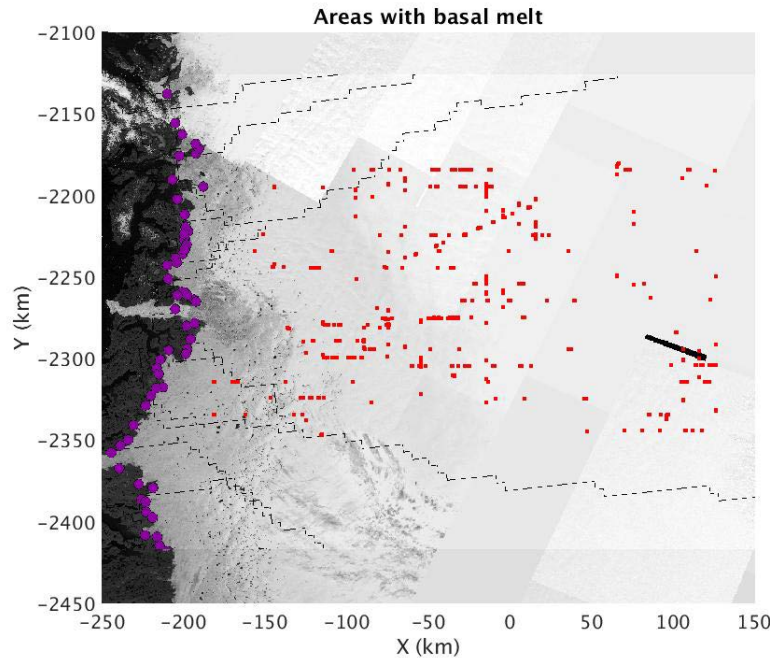


Figure 4.38 Areas of basal melt (red) in Jakobshavn Glacier, Purple dots show hydrological outlets (Lewis, 2009) and dotted lines show the hydrological sub-basin (Lewis, 2009)

The areas of basal melting are scattered and do not form any subglacial lake like structure. The deeper ice sheet bed is thawed because of pressure from the high thickness of ice sheet. Similarly, the basal melting may route towards the glacier calving front following the basal topography of the Jakobshavn. Here the hydrological sub-basins of Greenland have been plotted represented by dotted lines in Figure 4. 38, however, it has been calculated for whole Greenland scale and does not reveal the flow lines within the Jakobshavn catchment area (Lewis, 2009). The wet beds identified in this study can be used to identify the flow paths within the glacier.

4.3.4 Discussion and validation of ice bed reflectivity result

1. Crossover Analysis

The crossover analysis of Jakobshavn glacier in Fig. 4.39 (left) shows most of the areas to be pretty consistent with each other except the areas where the attenuation rate calculation fails to compensate for non-uniform changes in attenuation rates.

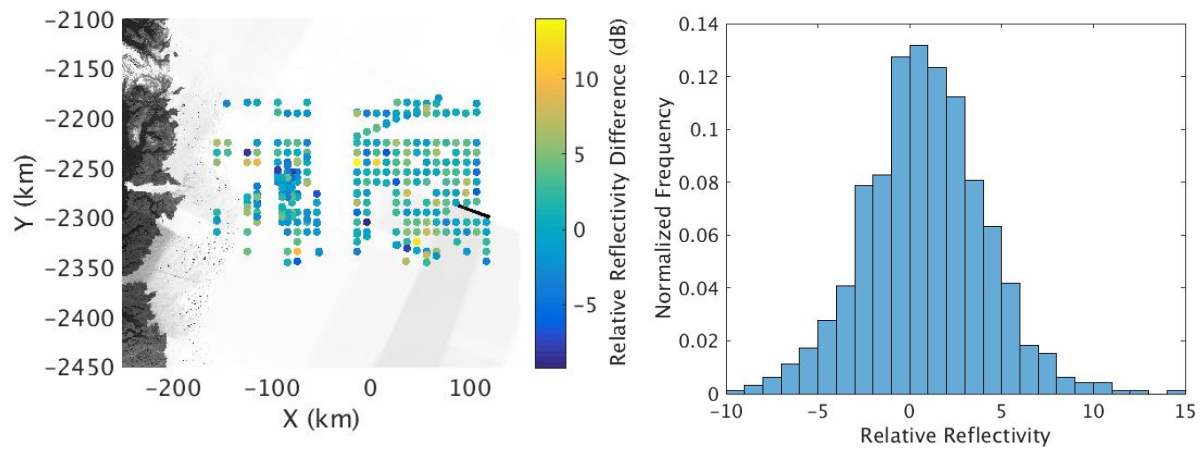


Figure 4.39 Relative Reflectivity Difference at crossovers (left), Relative Reflectivity Difference at crossovers (right)

The relative reflectivity difference at the crossovers is high shown in Fig. 4.39 (right) because of the quality of the bed echoes as mapping the bed in Jakobshavn glacier is difficult due to surface clutter and large attenuation by temperate ice and also due to the attenuation rate to be non-uniform towards the ice margins due to complex topographic features like crevasses and moulins. The crossover errors are within 86.84% within 5 dB and 67.67% within 3dB. However, the crossover match increased from 52% within 3 dB using uniform attenuation rate to 67.67% using variable attenuation method with interpolation at the longitudinal lines.

2. Geophysics

Figure 4.40 shows echogram for the area with higher reflectivity. The corresponding radar location and ice bed reflectivity are shown in the subfigures. The basal interface with high reflectivity has a relatively flat interface which can store or transfer the basal melt.

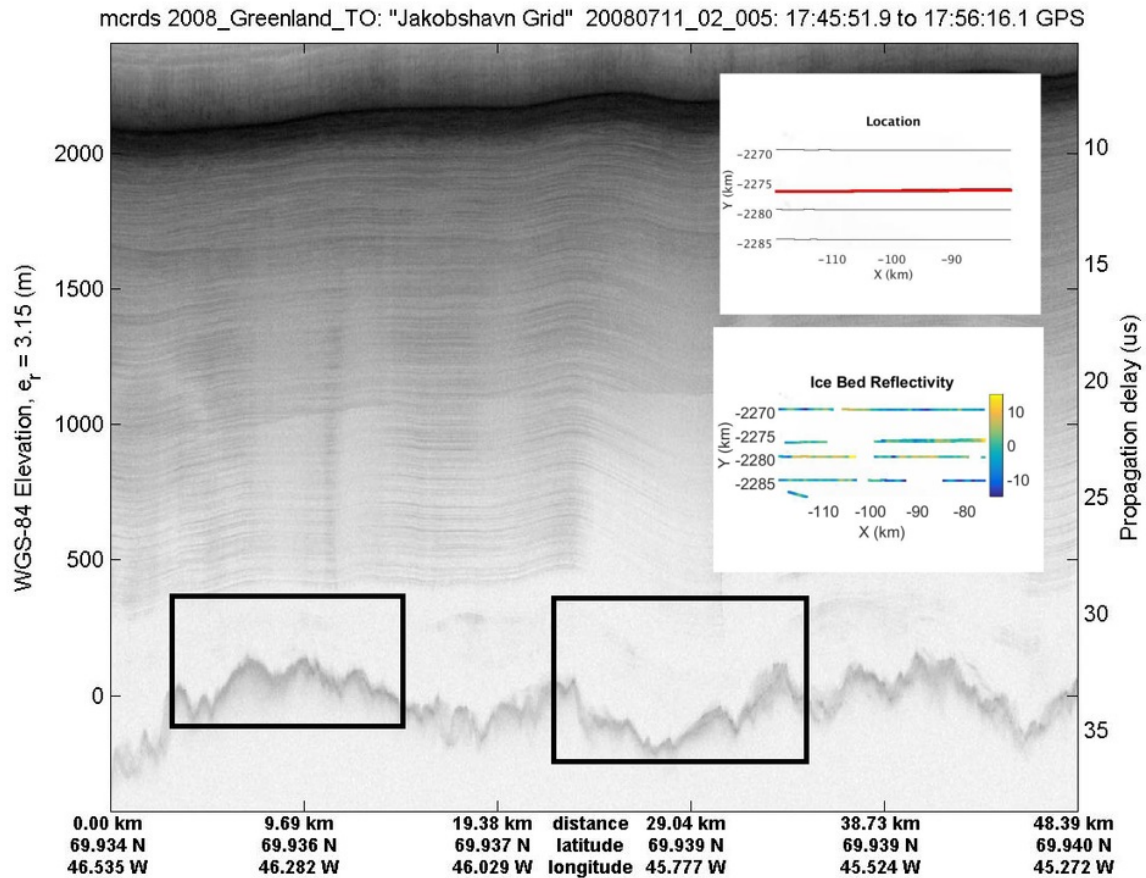


Figure 4.40 Echogram for 20080706_01_004

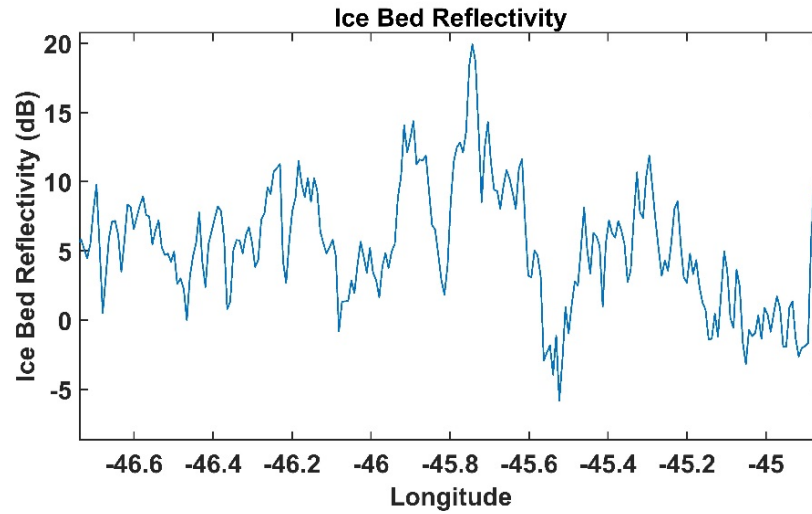


Figure 4.41 Ice Bed Reflectivity for 20080706_01_004

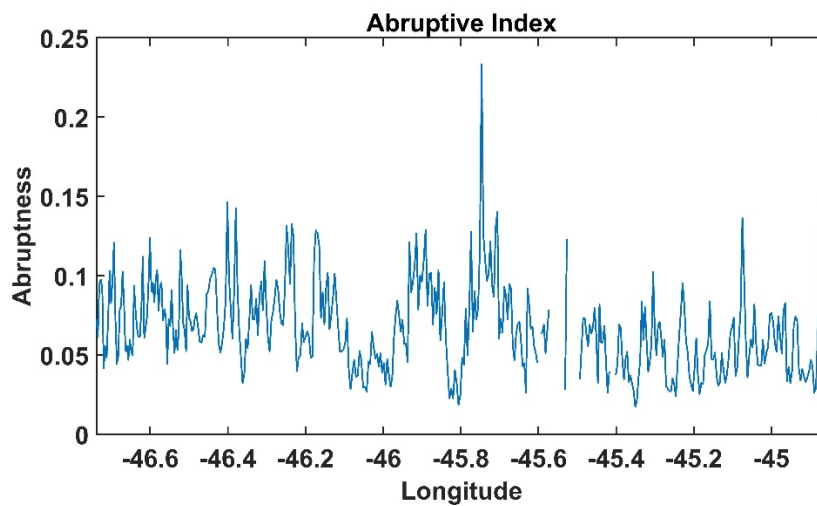


Figure 4.42 Abruptive Index for 20080706_01_004

Fig. 4.41 shows that the reflectivity is high corresponding to the area of high abruptness shown in Fig 4.42. Also the reflectivity is higher in the area that corresponds to flat interface, high dielectric contrast, relatively flat structure and high internal layers dipping.

3. Basal Melting and Bed Topography

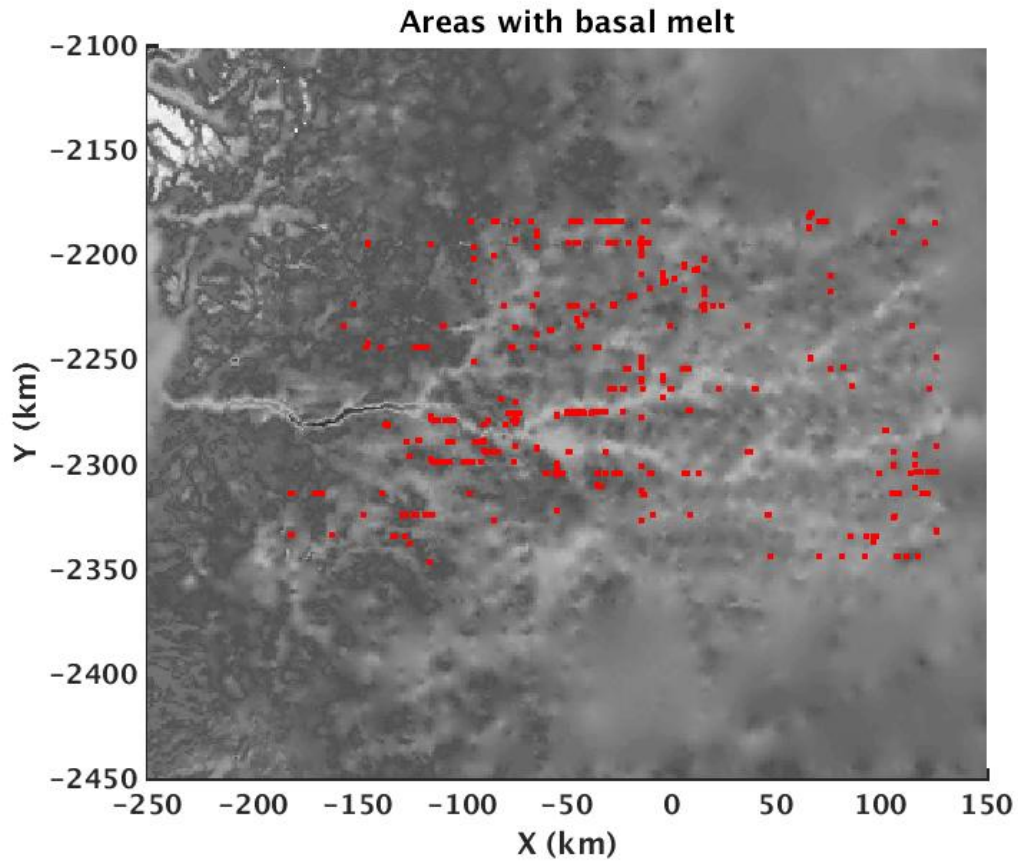


Figure 4.43 Areas with basal melt (red) from this study on top of ice bed map (Bamber, 2013)

The areas with higher reflectivity (greater than 10dB) are considered to be representative of basal melting (Chu et. al, 2016) shown by red areas in Fig. 4.43. As shown in Fig. 4.43, areas with basal melting shows basal melt to be scattered around the catchment area. The bed topography plays a crucial role in how this is routed along the glacier towards the calving front. Because of the topography, there is no formation of any subglacial lakes rather it lubricates the ice bed facilitating the ice flow towards the glacier front.

4. Comparison with Previous studies

It has been observed in previous studies that Jakobshavn glacier experiences large lateral and vertical shear forces and also experiences mass flux across its shear margins (Truffer and Echelmeyer, 2003). Van der Veen, Plummer, and Stearns (2011) assert that progressive shear margin weakening may contribute to the observed acceleration of Jakobshavn even though enhanced calving has been attributed to speed-up and mass losses (Bondzio et al., 2016; Podrasky et al., 2014; Sundal et al., 2013). In addition to this, Lampkin et al. 2013 observed that meltwater injection from water-filled crevasses weakens the shear margins, resulting in acceleration of ice flow into the ice stream. Hydrofracture often occurs when the storage capacity and water depths of these crevasses are large enough (Weertman, 1973; Lampkin et al., 2013).

Palmer observed that meltwater is generated at the surface of Greenland Ice sheet during summer and flows under the effect of gravity as supraglacial streams collecting at topographic lows forming supraglacial lakes. As melting continues through summer months these lakes and streams connect to englacial and subglacial pathways through moulins and crevasses. The subglacial water thus flows within the subglacial pathway towards the margin but the times it remains at the ice bed is unknown. It can be thus inferred that the basal melting towards the ice front could be due to surface meltwater injection while basal melting at deeper ice beds are the result of high pressure from thicker ice sheets.

It has been previously identified that the bed beneath the Jakobshavn isbrae near the calving front is largely thawed (Jordan, 2018). However, we observed that even the catchment area has basal melting scattered around which could have flowed towards the margin and lubricated the ice sheet causing higher ice flow rate towards the ice margin.

Chapter 5 Summary and Conclusion

5.1 Summary

In this study, the ice basal conditions of Petermann and Jakobshavn glacier have been studied using RES data. The ice bed reflectivity maps have been generated after compensating for geometrical spreading loss, rough interfaces, and englacial attenuation. Roughness estimation was done by applying Grima's Radar Statistical Reconnaissance (RSR) Method. This roughness estimation was validated using roughness calculated from Laser and Ku band radar data. The result reveals rougher areas of Petermann and Jakobshavn glacier which are in agreement with the features of the glaciers.

Englacial attenuation calculation was done using Schroeder's variable attenuation model. This works well with radar lines extending from deeper to shallower areas and linearly varying attenuation rate, however, fails when applied to regions with a sharp change in attenuation rate. Finally, the ice bed reflectivity map generated was used to infer the locations of basal melting where areas with higher reflectivity (greater than 10 dB) are interpreted as basal melting. Crossover analysis was done to check the ice bed reflectivity mismatch at crossover regions where it was observed to be consistent.

Abruptive index was used to validate the areas with higher reflectivity where higher abruptness corresponds to higher reflectivity. The geophysics of areas with basal melt was studied to reveal areas with high dielectric contrast, internal layers dipping and flat interfaces.

The areas with basal melt are also compared to the ice bed topography, hydraulic potential and ice surface velocity. Comparing with previous studies the reflectivity values are also consistent with some disagreement which comes from the limitations of the methods used.

Petermann glacier is found to have alternate basal melting and frozen beds. The glacier does not have topographic pinning and thus is subject to higher ice flow speed. On the other hand, Jakobshavn glacier has several areas of basal melt scattered in the catchment area with most concentrated towards the glacier front. The ice bed channels and retrograde slope in the glacier play important role in routing the subglacial water.

5.2 Conclusion and Future Works

This study reveals certain areas of basal melting that are localized in Petermann and Jakobshavn glaciers with previous studies focusing on whole Greenland ice sheet level view. The basal melting in these two glaciers are important in explaining the higher ice flow rate at these glaciers. Petermann glacier's alternate wet and frozen beds reveal the process of frictional heating by basal drag to ice melt formation and meltwater freezing by advective cooling thus controlling the onset of the glacier.

Jakobshavn high flow rate is majorly because of ocean induced melting and ice calving at the glacier front gradually weakening the ice margin, its bedrock geometry, and troughs which will continue to affect the glaciers ice mass loss in coming years. Jakobshavn glacier has abundant surface water infiltrations into the ice bed via moulins and crevasses which flow through complex drainage networks near the ice calving front. In addition, deeper areas of ice sheet also have scattered basal melting which is the result of thermal insulation and high pressure from thicker ice sheets.

The results here can be improved by using a better englacial attenuation calculation method which can compensate for the non-uniformly varying attenuation rates. Near the calving fronts, the ice bed echoes are affected by the complex ice surfaces and the geometry of the ice bed interface which brings some ice bed power loss. The results for basal water detection can be improved if a better englacial attenuation method is used or a method independent of englacial attenuation calculation like bed echo variability analysis (Jordan et al., 2018) is used.

References

- Allen, C., (2008), A brief history of radio – echo sounding of ice, <https://earthzine.org/2008/09/26/a-brief-history-of-radio-echo-sounding-of-ice>,
- Allen, C., (2017), Introduction to radar systems slides
- Baghdadi, N., King, C., Chanzy, A., Wigneron, J. P., (2002), An empirical calibration of the integral equation model based on SAR data soil moisture and surface roughness measurement over bare soils, *Int. J. Remote Sens.*, vol. 23, no. 20, pp. 4325-4340.
- Bamber, J. L., Layberry, R. L., and Gogineni, S. P., (2001), A new ice thickness and bed data set for the Greenland ice sheet: 1. Measurement, data reduction, and errors, *J. Geophys. Res.*, 106(D24), 33773–33780, doi: 10.1029/2001JD900054.
- Bentley, C. R., Lord, N. and Liu, C. (1998), Radar reflections reveal a wet bed beneath stagnant Ice Stream C and a frozen bed beneath ridge BC, West Antarctica, *J. Glaciol.*, 44(146), 149–156.
- Bindschadler, R. A. (1984), Jakobshavns Glacier drainage basin: A balance assessment, *J. Geophys. Res.*, 89(C2), 2066–2072, doi: 10.1029/JC089iC02p02066.
- Bondzio, J., Seroussi, H., Morlighem, M., Kleiner, T., Rückamp, M., Humbert, A., & Larour, E. (2016). Modeling calving front dynamics using a level-set method: Application to Jakobshavn Isbræ, West Greenland. *The Cryosphere*, 10(2), 497–510. <https://doi.org/10.5194/tc-10-497-2016>

- Brock, J. C., Krabill, B., Sallenger, A. H., Wright, C. W. and Swift, B. (2002), Basis and methods of NASA Airborne Topographic Mapper Lidar surveys for coastal studies *J. Coastal Res.*, 18(1), 1-13
- Chu, W., Schroeder, D. M., Seroussi, H., Creyts, T. T., & Bell, R. E. (2018), Complex basal thermal transition near the onset of Petermann Glacier, Greenland. *Journal of Geophysical Research: Earth Surface*, 123, 985–995. <https://doi.org/10.1029/2017JF004561>
- Church, J. A., Gregory, J. M., in *Climate Change 2001: The Scientific Basis*, J. T. Houghton et al., Eds. (Cambridge Univ. Press, Cambridge, 2001), chap. 11, pp. 641–693.
- CReSIS MCoRDS description, ftp://data.cresis.ku.edu/data/rds/rds_readme.pdf
- Dahl-Jensen, D., Gundestrup, N., Gogineni, S. P., and Miller, H., (2003), Basal melt at NorthGRIP modeled from borehole, ice-core and radio-echo sounder observations, *Annals of Glaciology*, 37, 207–212, doi: 10.3189/172756403781815492.
- Dowdeswell, J. A., & Evans, S. (2004). Investigations of the form and flow of ice sheets and glaciers using radio-echo sounding. *Reports on Progress in Physics*, 67(10), 1821–1861. <https://doi.org/10.1088/0034-4885/67/10/R03>
- Falkner, K. K., Melling, H., Münchow, A. M., Box, J. E., Wohlleben, T., Johnson, H. L., Gudmandsen, P., Samelson, R., Copland, Steffen, K., Rignot, E., Higgins, A. K., Context for the Recent Massive Petermann Glacier Calving Event, *Eos, Transactions American Geophysical Union* 92 (14) (2011) 117-118. Doi: 10.1029/2011EO140001.

- Fastook, J. L.; Brecher, H. H.; and Hughes, Terence J., Derived bedrock elevations, strain rates and stresses from measured surface elevations and velocities - Jakobshavns-Isbrae, Greenland (1995). Earth Science Faculty Scholarship. 27.
- Favier, L., Gagliardini, O., Durand, G., and Zwinger, T., (2011), A three dimensional full Stokes model of the grounding line dynamics: effect of a pinning point beneath the ice shelf, *The Cryosphere Discuss.*, 5, 1995–2033, doi: 10.5194/tcd-5-1995-2011.
- Fretwell, P., Pritchard, H. D., Vaughan, D. G., Bamber, J. L., Barrand, N. E., Bell, R., Bianchi, C., Bingham, R. G., Blankenship, D. D., Casassa, G., Catania, G., Callens, D., Conway, H., Cook, A. J., Corr, H. F. J., Damaske, D., Damm, V., Ferraccioli, F., Forsberg, R., Fujita, S., Gim, Y., Gogineni, P., Griggs, J. A., Hindmarsh, R. C. A., Holmlund, P., Holt, J. W., Jacobel, R. W., Jenkins, A., Jokat, W., Jordan, T., King, E. C., Kohler, J., Krabill, W., Riger-Kusk, M., Langley, K. A., Leitchenkov, G., Leuschen, C., Luyendyk, B. P., Matsuoka, K., Mouginot, J., Nitsche, F. O., Nogi, Y., Nost, O. A., Popov, S. V., Rignot, E., Rippin, D. M., Rivera, A., Roberts, J., Ross, N., Siegert, M. J., Smith, A. M., Steinhage, D., Studinger, M., Sun, B., Tinto, B. K., Welch, B. C., Wilson, D., Young, D. A., Xiangbin, C., and Zirizzotti, (2013), A., Bedmap2: improved ice bed, surface and thickness datasets for Antarctica, *The Cryosphere*, 7, 375-393, <https://doi.org/10.5194/tc-7-375-2013>.
- Fujita, S., Maeno, H., & Matsuoka, K. (2006). Radio wave depolarization and scattering within ice sheets: A matrix based model to link radar and ice core measurements and its application. *Journal of Glaciology*, 52(178), 407–424. <https://doi.org/10.3189/172756506781828548>

- Fung, A. K., and Chen, K. S., (2004), An update on the IEM surface backscattering model, IEEE Geosci. and Remote Sens. Lett. vol. 1 (2) pp. 75-77.
- Gogineni, S., Tammana, D., Braaten, D., Leuschen, C., Akins, T., Legarsky, J., Kanagaratnam, P., Stiles, J., Allen, C., and Jezek, K. (2001), Coherent radar ice thickness measurements over the Greenland ice sheet, J. Geophys. Res., 106(D24), 33761–33772, doi: 10.1029/2001JD900183.
- Gogineni, S., Yan, J. B., Gomez-Garcia, D., Rodriguez-Morales, F., Leuschen, C., Wang, Z., Paden, J., Hale, R., Arnold, E., Braaten, D., (2015), Ultra-wideband radars for measurements over ICE and SNOW, Geoscience and Remote Sensing Symposium (IGARSS) 2015 IEEE International, pp. 4204-4207.
- Gogineni, S., Yan, J., Paden, J., Leuschen, C., Li, J., Rodriguez-Morales, F., Gauch, J. (2014). Bed topography of Jakobshavn Isbræ, Greenland, and Byrd Glacier, Antarctica. Journal of Glaciology, 60(223), 813-833. doi: 10.3189/2014JoG14J129
- Gomez-Garcia, D., Rodriguez-Morales, F., Leuschen, C. and Gogineni, S., KU-Band radar altimeter for surface elevation measurements in polar regions using a wideband chirp generator with improved linearity, (2012), IEEE International Geoscience and Remote Sensing Symposium, Munich, 2012, pp. 4617-4620. doi: 10.1109/IGARSS.2012.6350437
- Greve, R., (1997), Application of a polythermal three-dimensional ice sheet model to the Greenland Ice Sheet: Response to Steady-State and Transient Climate Scenarios. J. Climate, 10, 901–918, [https://doi.org/10.1175/1520-0442\(1997\)010<0901:AOAPTD>2.0.CO;2](https://doi.org/10.1175/1520-0442(1997)010<0901:AOAPTD>2.0.CO;2).

- Grima, C., Blankenship, D. D., Young, D. A. and Schroeder, D. M. (2014), Surface slope control on firn density at Thwaites Glacier, West Antarctica: Results from airborne radar sounding, *Geophys. Res. Lett.*, 41, 6787–6794, doi: 10.1002/2014GL061635.
- Grima, C., Kofman, W., Herique, A., Orosei, R., Seu, R., (2012), Quantitative analysis of Mars surface radar reflectivity at 20MHz, *Icarus*, Volume 220, Issue 1, Pages 84-99, ISSN 0019-1035, <https://doi.org/10.1016/j.icarus.2012.04.017>.
- Gudmandsen, P. E. (1971), *Electromagnetic probing of the ice*, Golem Press, Boulder, Colo.
- Harvey, C., (2015), https://www.washingtonpost.com/news/energy-environment/wp/2015/08/19/one-of-the-worlds-fastest-melting-glaciers-may-have-just-lost-its-biggest-chunk-of-ice-ever/?utm_term=.a44bcb205327, Aug 9, 2015
- Helm, V., Humbert, A., Miller, H. (2014): Elevation model of Antarctica derived from CryoSat-2 in the period 2011 to 2013, links to DEM and uncertainty map as GeoTIFF. PANGAEA, <https://doi.org/10.1594/PANGAEA.831392>, In supplement to: Helm, V et al. (2014): Elevation and elevation change of Greenland and Antarctica derived from CryoSat-2. *The Cryosphere*, 8(4), 1539-1559, <https://doi.org/10.5194/tc-8-1539-2014>
- Jordan, T. M., Cooper, M. A., Schroeder, D. M., Williams, C. N., Paden, J. D., Siegert, M. J., and Bamber, J. L.,(2017), Self-affine subglacial roughness: consequences for radar scattering and basal water discrimination in northern Greenland, *The Cryosphere*, 11, 1247-1264, <https://doi.org/10.5194/tc-11-1247-2017>.
- Joughin, I., Smith, B., Howat, I., Scambos, T. and Moon, T., (2010). Greenland flow variability from ice-sheet-wide velocity mapping, *Journal of Glaciology*. 56. 415-430.

- Kanagaratnam, P., Gogineni, S. P., Ramasami, V. and Braaten, D., A wideband radar for high-resolution mapping of near-surface internal layers in glacial ice, in *IEEE Transactions on Geoscience and Remote Sensing*, vol. 42, no. 3, pp. 483-490, March 2004. doi: 10.1109/TGRS.2004.823451
- Kwok, R., Cunningham, G. F., Manizade, S. S. and Krabill, W. B. (2012), Arctic sea ice freeboard from IceBridge acquisitions in 2009: Estimates and comparisons with ICESat, *J. Geophys. Res.*, 117.
- Lampkin, D., Amador, N., Parizek, B., Farness, K., & Jezek, K. (2013). Drainage from water-filled crevasses along the margins of Jakobshavn Isbræ: A potential catalyst for catchment expansion. *Journal of Geophysical Research: Earth Surface*, 118, 795–813. <https://doi.org/10.1002/jgrf.20039>
- Leuschen, C., Gogineni, S. P., Hale, R., Paden, J., Rodriguez, F., Panzer, B., Gomez, D., IceBridge MCoRDS L1B Geolocated Radar echo strength profiles, Version 2, 2014 updated 2016.
- Lewis, S. (2009). Hydrologic outlets of the Greenland ice sheet, Version 1. Boulder, Colorado USA. NSIDC: National Snow and Ice Data Center. doi: <https://doi.org/10.5067/NBBVU83OJYY1>. [2018-08-14].
- Li, J., (2014), Unambiguous determination of ice sheet basal conditions from radio echo sounding data, NASA grant NNX14AL99G.
- Livingstone, S. J, Clark, C. D, Woodward, J. & Kingslake, J., (2013), Potential subglacial lake locations and meltwater drainage pathways beneath the Antarctic and Greenland ice sheets, *The Cryosphere*, vol. 7, no. 6, pp. 1721–1740.

- Macdonald, G., Banwell, A., & MacAyeal, D. (2018). Seasonal evolution of supraglacial lakes on a floating ice tongue, Petermann Glacier, Greenland. *Annals of Glaciology*, 59(76pt1), 56-65. doi:10.1017/aog.2018.9
- MacGregor, J. A., Catania, G. A., Conway, H., Schroeder, D. M., Joughin, I., Young, D. A., Kempf, S. D., and Blankenship, D. D., (2013), Weak bed control of the eastern shear margin of Thwaites Glacier, West Antarctica, *J. Glaciol.*, 59, 900–912, doi:10.3189/2013JoG13J050.
- MacGregor, J. A., et al. (2016), A synthesis of the basal thermal state of the Greenland Ice Sheet, *J. Geophys. Res. Earth Surf.* 121, 1328–1350, doi: 10.1002/2015JF003803.
- Malyala, S. K., Li, J., Adhikari, M., Morales, F. R., Estimation of ice basal reflectivity of Byrd glacier using RES data, (2017), *IEEE International Geoscience and Remote Sensing Symposium*, Fort Worth, TX, 2017, pp. 2836-2839, doi: 10.1109/IGARSS.2017.8127589.
- Middleton, D., (2012), *The Year Greenland Melted (AKA Alarmists Gone Wild)*, wattsupwiththat.com
- Moon, T. and Joughin, I. (2008), Changes in ice front position on Greenland's outlet glaciers from 1992 to 2007. *J. Geophys. Res.*, 113(F2), F02022 (doi: 10.1029/2007JF000927)
- Münchow, A., Padman, L., Fricker, H. A., Interannual changes of the floating ice shelf of Petermann Gletscher, North Greenland, from 2000 to 2012, *Journal of Glaciology* 60 (221) (2014) 489-499. doi: 10.3189/2014JoG13J135.
- NASA ATM Image, (2009), <https://atm.wff.nasa.gov/>

- Neal, C. S. (1979), The dynamics of the Ross Ice Shelf revealed by radio echo-sounding, *J. Glaciol.*, 24(90), 295– 307.
- Neal, C. S. (1982), Radio echo determination of basal roughness characteristics on the Ross Ice Shelf, *Ann. Glaciol.*, 3, 216– 221.
- Nick, F., Luckman, A., Vieli, A., Van Der Veen, C., Van As, D., Van De Wal, R., Floricioiu, D. (2012). The response of Petermann Glacier, Greenland, to large calving events, and its future stability in the context of atmospheric and oceanic warming. *Journal of Glaciology*, 58(208), 229-239. doi: 10.3189/2012JoG11J242
- Oswald, G. and Gogineni, S., (2008), Recovery of subglacial water extent from Greenland radar survey data, *Journal of Glaciology*, 54, 94–106, doi:10.3189/002214308784409107.
- Oswald, G. K. A. (1975), Investigation of sub-ice bedrock characteristics by radio-echo sounding, *J. Glaciol.*, 15(73), 75–87.
- Oswald, G. K. A., and Robin, G de Q., (1973), Lakes beneath the Antarctic Ice Sheet, *Nature*, 245(5423), 251– 254.
- Palmer, S. J., Dowdeswell, J. A., Christoffersen, P., Young, D., Blankenship, D. D., Greenbaum, J. S., Benham, T., Bamber, J. and Siegert, M. J. (2013), Greenland subglacial lakes detected by radar, *Geophys. Res. Lett.*, 40, 6154–6159, doi: 10.1002/2013GL058383.
- Peters, M. E., Blankenship, D. D. and Morse, D. L. (2005), Analysis techniques for coherent airborne radar sounding: Application to West Antarctic ice streams, *J. Geophys. Res.*, 110, B06303, doi: 10.1029/2004JB003222.

- Podrasky, D., Truffer, M., Lüthi, M., & Fahnestock, M. (2014). Quantifying velocity response to ocean tides and calving near the terminus of Jakobshavn Isbræ, Greenland. *Journal of Glaciology*, 60(222), 609–621. <https://doi.org/10.3189/2014JoG13J130>
- Rahman, M. M., Moran, M. S., Thoma, D. P., Bryant, R., Holifield Collins, C. D., Jackson, T., Orr, B. J., Tischler, M., Mapping surface roughness and soil moisture using multi-angle radar imagery without ancillary data, *Remote Sensing of Environment*, Volume 112, Issue 2, 2008, Pages 391-402, ISSN 0034-4257, <https://doi.org/10.1016/j.rse.2006.10.026>.
- Rennermalm, A. K., Moustafa, S. E., Mioduszewski, J., Chu, V. W., Forster, R. R., Hagedorn, B., Harper, J. T., Mote, T. L., Robinson, D. A., Shuman, C. A., Smith, L. C., and Tedesco, M., (2013), Understanding Greenland ice sheet hydrology using an integrated multi-scale approach, *Environmental Research Letters*, 8, 015 017, doi:10.1088/1748-9326/8/1/015017.
- Rignot, E., Gogineni, S., Joughin, I. and Krabill, W. (2001) Contribution to the glaciology of northern Greenland from satellite radar interferometry. *J. Geophys. Res.*, 106(D24), 34 007–34 019
- Rignot, E., Mouginot, J., Larsen, C., Gim, Y., and Kirchner, D., Low-frequency Radar sounding of temperate ice masses in Southern Alaska, *Geophysical Research Letters*. 40. 5399-5405. <https://doi.org/10.1002/2013GL057452>er, J. L., Griggs, J. A., Hurkmans, R. T. W. L., Dowdeswell, J. A., Gogineni, S. P., Howat, I., Mouginot, J., Paden, J., Palmer, S., Rignot, E., and Steinhage, D., A new bed elevation dataset for Greenland, *The Cryosphere*, 7, 499-510, <https://doi.org/10.5194/tc-7-499-2013>, 2013.

- Rignot, E., Steffen, K., Channelized bottom melting and stability of floating ice shelves, *Geophysical Research Letters* 35 (L02503) (2008) 1-5. doi: 10.1029/2007GL031765.
- Rippin, D. (2013). Bed roughness beneath the Greenland ice sheet. *Journal of Glaciology*, 59(216), 724-732. doi: 10.3189/2013JoG12J212
- Robin, G. de Q., Drewry, D. J. and Meldrum, D. T., (1977), International studies of ice sheet and bedrock, *Philos. Trans. R. Soc. London, Ser. B*, 279, 185– 196.
- Rodríguez-Morales, F. et al., Advanced multifrequency radar instrumentation for polar research, *IEEE Trans. Geosci. Remote Sens.*, 52(5), 2824–2842, 2014, doi:10.1109/TGRS.2013.2266415.
- Rutt, I. C., Hagdorn, M., Hulton, N. R. J. and Payne, A. J., (2009), The Glimmer community ice sheet model, *J. Geophys. Res.*, 114, F02004, doi: 10.1029/2008JF001015.
- Lewis, S., (2009). Hydrologic Sub-basins of Greenland, Version 1. Boulder, Colorado USA. NSIDC: National Snow and Ice Data Center. doi: <https://doi.org/10.5067/DT9T7DPD7HBI>. [2018-08-14]
- Sasha, P. C., (2008), Evolving subglacial water systems in East Antarctica from Airborne Radar Sounding, Ph. D. Thesis, University of Texas at Austin.
- Schroeder, D. M., Grima, C. and Blankenship, D. D. (2016), Evidence for variable grounding-zone and shear-margin basal conditions across Thwaites Glacier, West Antarctica.”*GEOPHYSICS*, 81(1), WA35-WA43. <https://doi.org/10.1190/geo2015-0122.1>

- Schroeder, D., Seroussi, H., Chu, W., & Young, D. (2016). Adaptively constraining radar attenuation and temperature across the Thwaites Glacier catchment using bed echoes. *Journal of Glaciology*, 62(236), 1075-1082. doi:10.1017/jog.2016.100
- Schutz, B. E., Zwally, H. J., Shuman, C. A., Hancock, D., and DiMarzio, J. P., (2005), Overview of the ICESat Mission, *Geophys. Res. Lett.*, 32, L21S01, doi: 10.1029/2005GL024009.
- Seroussi, H., Morlighem, M., Rignot, E., Khazendar, A., Larour, E., & Mouginot, J. (2013). Dependence of century-scale projections of the Greenland ice sheet on its thermal regime. *Journal of Glaciology*, 59(218), 1024-1034. doi: 10.3189/2013JoG13J054
- Shepherd, A., Ivins, E., Barletta, G. A. V., Bentley, M. J., Bettadpur, S., Briggs, K. H., Bromwich, D. H., Forsberg, R., Galin, N., Horwath, M., Jacobs, S., Joughin, I., King, M. A., Lenaerts, J. T. M., Li, J., Ligtenberg, S. R. M., Luckman, A., Luthcke, S. B. et al., (2012), A reconciled estimate of ice-sheet mass balance, *Science* 338(6111), 1183–1189 (DOI: 10.1126/science.1228102).
- Smith, A.M., Murray, T., Bedform topography and basal conditions beneath a fast-flowing West Antarctic ice stream, *Quaternary Science Reviews*, Volume 28, Issues 7-8, 2009, Pages 584-596, ISSN 0277-3791, <https://doi.org/10.1016/j.quascirev.2008.05.010>.
- Studinger, M. S. 2014, updated 2017. IceBridge ATM L2 Icessn Elevation, Slope, and Roughness. Version 2. [2012-2014]. Boulder, Colorado USA: NASA DAAC at the National Snow and Ice Data Center. <http://dx.doi.org/10.5067/CPRXXK3F39RV>. [2017].
- Studinger, M., Koenig, L., Martin S. and Sonntag, J., Operation icebridge: Using instrumented aircraft to bridge the observational gap between icesat and icesat-2, (2010), IEEE

- International Geoscience and Remote Sensing Symposium, Honolulu, HI, 2010, pp. 1918–1919. doi: 10.1109/IGARSS.2010.5650555.
- Sundal, A., Shepherd, A., Broeke, M., Angelen, J., Gourmelen, N., & Park, J. (2013). Controls on short-term variations in Greenland glacier dynamics. *Journal of Glaciology*, 59(217), 883–892. <https://doi.org/10.3189/2013jog13j019>
- Taylor, J., Siegert, M. J., Payne, A. J., Hubbard, B. Regional-scale bed roughness beneath ice masses: measurement and analysis, In *Computers & Geosciences*, Volume 30, Issue 8, Pages 899–908, ISSN 0098-3004, 2004, <https://doi.org/10.1016/j.cageo.2004.06.007>.
- Truffer, M., & Echelmeyer, K. (2003). Of isbrae and ice streams. *Annals of Glaciology*, 36, 66–72. <https://doi.org/10.3189/172756403781816347>
- Ulaby, F.T., Moore, R.K., Fung, A.K., (1986). *Microwave Remote Sensing: Active and Passive, from Theory to Applications*. Artech House Publishers. ISBN 0890061920.
- Uratsuka, S., Nishio, F. and Mae, S. (1996), Internal and basal ice changes near the grounding line derived from radio echo sounding, *J. Glaciol.*, 42(140), 103–109.
- van der Veen, C. J., *Fundamentals of Glacier dynamics*, (2013), Chap. 6, Taylor and Francis, 2 edition.
- Van der Veen, C., Plummer, J., & Stearns, L. (2011), Controls on the recent speed-up of Jakobshavn Isbræ, West Greenland. *Journal of Glaciology*, 57(204), 770–782. <https://doi.org/10.3189/002214311797409776>
- Weertman, J. (1973). Creep of Ice. In E. Whalley, S. J. Jones, & L. W. Gold (Eds.), *Physics and Chemistry of Ice*, (320–337). Ottawa: Royal Society of Canada.

Young, D. A., Schroeder, D. M., Blankenship, D. D., Kempf, S. D., and Quartini, E., The distribution of basal water between Antarctic subglacial lakes from radar sounding, (2016), Phil. Trans. R. Soc. A., 374, doi:10.1098/rsta.2014.0297.

Zribi, M ., Dechambre, M., A new empirical model to retrieve soil moisture and roughness from C-band radar data, Remote Sensing of Environment, Volume 84, Issue 1, (2003), Pages 42-52, ISSN 0034-4257, [https://doi.org/10.1016/S0034-4257\(02\)00069-X](https://doi.org/10.1016/S0034-4257(02)00069-X).